Inorganic Chemistry
Article

Influence of the Redox Active Ligand on the Reactivity and Electronic Structure of a Series of Fe(TIM) Complexes

Corinna R. Hess,[†] Thomas Weyhermüller, Eckhard Bill, and Karl Wieghardt*

Max Planck Institut für Bioanorganische Chemie, 45470 Mülheim an der Ruhr, Germany. [†]Current address: Department of Chemistry, Durham University, South Road, Durham, DH1 3LE, United Kingdom.

The redox properties of Fe and Zn complexes coordinated by an α-diimine based N_4-macrocyclic ligand (TIM) have been examined using spectroscopic methods and density functional theory (DFT) computational analysis. DFT results on the redox series of $[Zn(TIM^*)]^n$ and $[Fe(TIM^*)]^n$ molecules indicate the preferential reduction of the α-diimine ligand moiety. In addition to the previously reported $[Fe(TIM^*)]_2$ dimer, we have now synthesized and characterized a further series of monomeric and dimeric complexes coordinated by the TIM ligand. This includes the five-coordinate monomeric $[Fe(TIM^*)I]$, the neutral and cationic forms of a monomeric phosphite adduct, $[Fe(TIM^*)(P(OPh)_3)]$ and $[Fe(TIM^*)(P(OPh)_3)](PF_6)$, as well as a binuclear hydroxy-bridged complex, $[\{Fe(TIM^*)\}_2(\mu\text{-OH})](PF_6)$. Experimental and computational data for these synthetic compounds denote the presence of ferrous and ferric species, suggesting that the α-diimine based macrocycles do not readily support the formation of formally low-valent (M^0 or M^I) metal complexes as previously speculated. Magnetochemical, Mössbauer, electron paramagnetic resonance (EPR), and electronic spectral data have been employed to experimentally determine the oxidation state of the central metal ion and of the macrocyclic ligand (TIM*) in each compound. The series of compounds is described as follows: $[Fe^{II}(TIM^0)(CH_3CN_2)]^{2+}$, $S_{Fe} = S_T = 0$; $[Fe^{2.5}(TIM^{2.5-})]_2$, $S_T = 1$; $[\{Fe^{III}(TIM^{2-})\}_2(\mu\text{-OH})]^+$, $S_{Fe} = 3/2$, $S_T = 0$; $[Fe^{III}(TIM^{2-})I]$, $S_{Fe} = 3/2$, $S_T = 1/2$; $[Fe^{II}(TIM^{2-})(P(OPh)_3)]$, $S_{Fe} = S_T = 0$; and $[Fe^{II}(TIM^{1-})(P(OPh)_3)]^{1+}/[Fe^{I}(TIM^0)(P(OPh)_3)]^{1+}$, $S_T = 1/2$. The results have been corroborated by DFT calculations.

1. Introduction

An extensive literature has been devoted to the chemistry of metal complexes coordinated by synthetic tetradentate N_4-macrocycles.[1] These ligands provided simple synthetic analogues of related biological molecules, such as hemes and cobalamin. Unsaturated macrocyclic α-diimine metal complexes in particular (e.g., tetraeneN$_4$* and TIM*,[2] Scheme 1) have proven to be broadly reactive, and have been targeted for a wide range of chemical transformations including dioxygen activation,[1,3] CO_2 reduction,[4,5] and alkyl transfer[6,7]

reactions. Most recently, cobalt tetraimine complexes have been exploited as hydrogen production catalysts.[8,9]

While the chemistry of the neutral macrocyclic α-diimine complexes is well-established, it is far from complete. Studies pertaining to ligand-centered redox processes of these molecules are particularly lacking, in comparison with analogous studies on porphyrin ligands.[10,11] Similar to the porphyrin systems, however, evidence points to the redox non-innocence of α-diimine-based macrocycles. Both Rose and Busch noted the presence of low-lying ligand-centered π^*-orbitals in Ni-(TIM) and Fe(tetraeneN$_4$) complexes that might favor reduction of the macrocycle.[12,13] Reduction of $[Ni^{II}(TIM^0)]^{2+}$

*To whom correspondence should be addressed. E-mail: wieghardt@mpi-muelheim.mpg.de. Phone: +49 (0)208 306-3610. Fax: +49 (0)208 306-3952.

(1) Endicott, J. F.; Durham, B. In *Coordination Chemistry of Macrocyclic Compounds*; Melson, G. A., Ed.; Plenum Press: New York, 1979; pp 393−460.

(2) We will designate the macrocycles as TIM* and tetraeneN$_4$* when used in a generic sense, irrespective of their true oxidation state (ranging from 0 to 4−).

(3) Wong, C.-L.; Switzer, J. A.; Balakrishnan, K. P.; Endicott, J. F. *J. Am. Chem. Soc.* **1980**, *102*, 5511.

(4) Fujita, E.; Brunschwig, B. S.; Ogata, T.; Yanagida, S. *Coord. Chem. Rev.* **1994**, *132*, 195.

(5) Schmidt, M. H.; Miskelly, G. M.; Lewis, N. S. *J. Am. Chem. Soc.* **1990**, *112*, 3420.

(6) Shi, S.; Bakac, A.; Espenson, J. H. *Inorg. Chem.* **1991**, *30*, 3410.

(7) Bakac, A.; Espenson, J. H. *Inorg. Chem.* **1989**, *28*, 4319.

(8) Hu, X.; Brunschwig, B. S.; Peters, J. C. *J. Am. Chem. Soc.* **2007**, *129*, 8988.

(9) Fihri, A.; Artero, V.; Razavet, M.; Baffert, C.; Leibl, W.; Fontecave, M. *Angew. Chem., Int. Ed.* **2008**, *47*, 564.
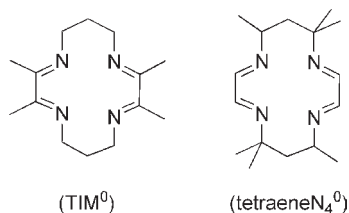
(10) *Synthesis and Organic Chemistry*; Kadish, K. M., Smith, K. M., Guilard, R., Eds.; Academic Press: New York, 2000; Vol. *1*.

(11) Floriani, C.; Floriani-Moro, R. In *Inorganic, Organometallic and Coordination Chemistry*; Kadish, K. M., Smith, K. M., Guilard, R., Eds.; Academic Press: New York, 2000; Vol. *3*, pp 405−421.

(12) Lovecchio, F. V.; Gore, E. S.; Busch, D. H. *J. Am. Chem. Soc.* **1974**, *96*, 3109.

(13) Norman, J. G. J.; Chen, L. M.; Perkins, C. M.; Rose, N. J. *Inorg. Chem.* **1981**, *20*, 1403.

Scheme 1

(TIM^0)   (tetraeneN$_4{}^0$)

Scheme 2. Oxidation Levels of α-Diimine Ligands[a]

[a] Average bond distances given in red in Å.

to generate the monocation, [Ni^{II}(TIM^{1-})]$^{1+}$, containing a ligand radical anion, (TIM^{1-}), has been established.[12] In contrast, reduction of [Fe(tetraeneN$_4$)(CH$_3$CN)$_2$]$^{2+}$ was reported to yield low valent Fe^I and Fe^0 species.[14]

Recent studies have unequivocally established the redox non-innocence of the fundamental building block of the tetraeneN$_4$ and TIM ligands, namely, the unsaturated α-diimine unit.[15−18] Redox studies on a variety of 4- or 5-coordinate first row transition metal complexes coordinated by iminopyridine and α-diimine ligands have demonstrated the tendency of the organic molecules, rather than the metal center, to acquire electrons. Spectroscopic, computational, and crystallographic data have provided clear evidence for ligand radicals in these systems. Crystal structures have proven particularly informative with regard to the ligand oxidation state; concrete changes in the α-diimine C−C and C−N bond distances are observed with each successive reduction (Scheme 2). Consequently, a theoretical 4e- redox series is available to the macrocyclic α-diimines, TIM and tetraeneN$_4$, which are expected to compete with metal centered redox processes in their coordination complexes. This factor is pertinent to the recent focus on Co-containing tetraimine systems as hydrogen evolution catalysts, since low-valent Co^I species have been invoked in the catalytic cycle.[8] Ligand based redox processes also provide an alternative formulation of Busch's low valent Fe^0 and Fe^I complexes.[14] A greater understanding of the nature of the redox processes in metal-coordinated α-diimine macrocycles may provide key insight into the unique reactivities of these systems.

To address such issues, we have focused our studies on the redox chemistry and reactivity of Fe complexes coordinated by the TIM* ligand. We recently reported on the formation of an unprecedented Fe−Fe dimer, [Fe(TIM*)]$_2$, generated upon reduction of [Fe^{II}(TIM^0)(MeCN)$_2$]$^{2+}$ with sodium in tetrahydrofuran (THF).[19] The dimer has an $S = 1$ ground state and possesses a weak unsupported Fe−Fe bond (bond order = 0.5). Spectroscopic and computational studies on the dimeric product clearly established the redox non-innocence of the TIM* ligands; the presence of TIM$^{2.5-}$ ligand radicals in [Fe(TIM*)]$_2$ was deemed largely accountable for the remarkable structure and magnetism of the dimer. These findings prompted us to further investigate the redox chemistry of the Fe(TIM*) system and to examine the effects of

ligand-centered redox processes on the electronic structure and reactivity of the Fe-containing compounds. Toward this effort, we now have carried out detailed computational studies on a series of monomeric Zn and Fe species coordinated by the TIM* ligand. The results establish clear structural trends across the series, which assist in the electronic structure characterization of M(TIM*) complexes. We also have investigated the reactivity of the Fe dimer toward several small molecules: I$_2$, PR$_3$, and O$_2$. The product Fe-(TIM*) complexes all comprise reduced TIM* ligands in various oxidation states (Scheme 3), again corroborating the redox non-innocence of the macrocyclic diimines. The isolation of low spin and intermediate spin ferrous and ferric complexes points to the ability to stabilize a variety of unique electronic structures. We have not found any evidence for the presence of genuine low-valent Fe^I or Fe^0 complexes in the series of Fe(TIM*) compounds, with a genuine d^7 or d^8 electronic configuration.

2. Experimental Section

Syntheses were carried out under an inert atmosphere, using standard Schlenk and glovebox techniques. Solvents (Fluka or Sigma-Aldrich) were dried and deoxygenated prior to use. Reagents were purchased from Sigma-Aldrich.

Bis(pentamethylcyclopentadienyl)iron hexafluorophosphate, [FeCp*$_2$]PF$_6$, was synthesized by oxidation of FeCp*$_2$ using 1 equiv of AgPF$_6$ in acetonitrile. The resultant green solution was filtered, and the solvent was removed in vacuo. The solid product was used without further purification.

Synthesis. [Zn^{II}(TIM^0)Cl](PF$_6$) (1). Compound 1 was prepared from [Cu^{II}(TIM^0)]ZnCl$_4$ according to a previously published procedure.[20] Single crystals were obtained by slow diffusion of ether into a solution of 1 in acetonitrile. Anal. Calcd for C$_{14}$H$_{24}$ClF$_6$N$_4$PZn: C, 34.01; H, 4.86; N, 11.33. Found: C, 34.05; H, 5.12; N, 11.33. ^{1}H NMR (CDCl$_3$), ppm: 2.07 (d, 2H), 2.25, (s, 12H), 2.97 (q, 2H), 3.63, (t, 2H), 3.86 (d, 2H).

[Fe^{II}(TIM^0)(MeCN)$_2$](PF$_6$)$_2$ (2) and [Fe(TIM*)]$_2$ (3) were prepared as previously described.[19]

[{Fe(TIM*)}$_2$(μ-OH)](PF$_6$) (4). Compound 4 was prepared from solutions of 2, as follows: 2.5 equiv of Na (as 5% Na/Hg beads = 100 mg Na/Hg = 0.217 mmol Na) was added to a suspension of 0.059 g (0.088 mmol) of 2 in ~11 mL of THF. After 24 h stirring, the crude mixture was filtered to remove Hg and Na salts, and transferred to a Schlenk flask. Assuming that all of the starting compound, [Fe^{II}(TIM^0)(MeCN)$_2$](PF$_6$)$_2$, was converted to [Fe(TIM*)]$_2$, then 0.51 equiv of dioxygen (2.25 × 10^{-5} mol O$_2$, added as 2.6 mL of air, 23 °C, 1 atm) was added via syringe, and the solution was stirred for 30 min, during which time the color changed to purple. The sample was placed under partial vacuum, and the solution was transferred to the glovebox and filtered. Yield: 100% conversion, as determined by UV−vis, using the absorbance at λ_{max} = 511 nm. Mössbauer analysis on the crude solid product mixture also shows clean conversion

(14) Rakowski, M. C.; Busch, D. H. *J. Am. Chem. Soc.* **1975**, *97*, 2570–2571.

(15) Lu, C. C.; Bill, E.; Weyhermüller, T.; Bothe, E.; Wieghardt, K. *J. Am. Chem. Soc.* **2008**, 130.

(16) Ghosh, M.; Weyhermüller, T.; Wieghardt, K. *Dalton Trans.* **2008**, 5149.

(17) Chlopek, K.; Muresan, N.; Neese, F.; Wieghardt, K. *Chem.—Eur. J.* **2007**, *13*, 8390.

(18) Muresan, N.; Chlopek, K.; Weyhermüller, T.; Neese, F.; Wieghardt, K. *Inorg. Chem.* **2007**, *46*, 5327.

(19) Hess, C. R.; Weyhermüller, T.; Bill, E.; Wieghardt, K. *Angew. Chem., Int. Ed.* **2009**, 48.

(20) Jackels, S. C.; Ciavola, J.; Carter, R. C.; Cheek, P. L.; Pascarelli, T. D. *Inorg. Chem.* **1983**, *22*, 3956.

(> 90% purity, Supporting Information). Crystals of **4** were obtained by slow diffusion of ether into the crude product mixture. Anal. Calcd for $C_{28}H_{49}F_6Fe_2N_8OP$: C, 43.65; H, 6.41; N, 14.54. Found: C, 43.99; H, 6.67; N, 14.09. UV−vis: λ_{max}, nm (ε M^{-1} cm^{-1}) in THF: 277 (23,400), 511 (10,650), 668 (3500), 744 (sh).

[Fe(TIM*)I] (5). I_2 (0.018 g, 0.071 mM) was added to a solution of **3** (0.043 g, 0.071 mM) in ~5 mL of THF, whereupon the color immediately turned purple. After several hours reaction time, the solution was subsequently filtered, and the solvent removed under vacuum. Yield: 82% Single crystals were obtained by slow diffusion of ether into a saturated solution of **5** in THF. Anal. Calcd for $C_{14}H_{24}FeIN_4$: C, 39.00; H, 5.61; N, 13.00. Found: C, 38.98; H, 5.57; N, 12.92. UV−vis: λ_{max} nm (ε M^{-1} cm^{-1}) in THF: 403 (4800), 537 (8900), 674 (3900), 745 (sh).

[Fe(TIM*)(P(OPh)$_3$)] (6). In a typical procedure, triphenylphosphite (2.14 equiv, 47 μL = 0.18 mmol) was added to a solution of **3** (0.051 g, 0.084 mmol) in 5 mL of THF, upon which the color immediately turned a turquoise-green. The reaction was allowed to stir overnight, and the solvent was removed under vacuum. The crude product was redissolved in hexane, filtered to remove any insoluble materials, and the dark turquoise filtrate was concentrated ~2−3 fold. Single crystals were obtained by cooling (−19 °C) the saturated solution of the product in hexane. Yield: 65% Anal. Calcd for $C_{32}H_{39}FeN_4O_3P$: C, 62.55; H, 6.40; N, 9.12. Found: C, 62.56; H, 6.35; N, 9.09.UV−vis: λ_{max} nm (ε M^{-1} cm^{-1}) in hexane: 264 (12,500), 412 (9200), 450 (5600), 590 (12,000), 892 (400). ^{1}H NMR (THF-d_6), ppm: 1.67, (s, 6H) 1.68 (s, 6H), 2.06 (m, 2H), 3.08 (m, 2H), 3.31, (m, 4H), 3.62 (m, 4H), 6.74 (d, 6H), 6.82 (t, 3H), 7.03 (t, 6H).

[Fe(TIM*)(P(OPh)$_3$)](PF$_6$) (7). To a solution of **6** (0.03 g, 0.049 mmol) in THF (10 mL) was added 1 equiv of [FeCp*$_2$](PF$_6$) (0.023 g, 0.049 mmol). The reaction mixture was stirred for 2 h, during which time the color became dark purple. The solution was filtered, and the solvent removed under vacuum. The crude product was washed with hexane to remove FeCp*$_2$ and any unreacted starting materials. Yield: 50%. Single crystals could be obtained from slow diffusion of hexane into a THF solution of the product. Repeated attempts to obtain a reasonable elemental analysis of this compound were unsuccessful; we suspect that this complex is unstable in the commercially available pyrolysis process. However, Mössbauer analysis of the crude material (Figure 12) obtained as described from the reaction of **6** with FeCp*$_2$ indicates clean conversion to a single Fe-containing product. This is further supported by its X-ray powder diffraction spectrum shown in Supporting Information, Figure S11, which is identical with the simulated spectrum derived from the single crystal analysis.

Physical Measurements. Elemental analyses were carried out by the Microanalytical Laboratory, Kolbe & Springer, Mülheim an der Ruhr, Germany. Electronic spectra were recorded on a Perkin-Elmer double-beam spectrometer. ^{1}H NMR spectra were collected on a Varian Mercury 400 MHz instrument. Electrochemical measurements were carried out using an EG&G potentiostat/galvanostat, glassy carbon working electrode, Ag/AgNO$_3$ reference electrode, and Pt wire as the counter electrode. Potentials are reported versus ferrocenium/ferrocene. Magnetic susceptibility data were recorded on an MPMS Quantum Design SQUID magnetometer (1.0 T, 2−300 K). Susceptibility data were corrected for underlying diamagnetism using tabulated Pascal's constants. X-band electron paramagnetic resonance (EPR) spectra were collected on a Bruker ESP 300 spectrometer. Mössbauer data were recorded on alternating constant-acceleration spectrometers. The minimum experimental line width was 0.24 mm s^{-1} (full width at half-height). The sample temperature was maintained constant in an Oxford Instruments Variox or an Oxford Instruments Mössbauer-Spectromag 2000 cryostat; the latter was used for measurements in applied magnetic fields with the field at the sample oriented perpendicular to the γ-beam. Isomer shifts are quoted relative to iron metal at 300 K. Data simulation was carried out using the programs "JulX" (SQUID), and "MFIT" (Mössbauer) by E. Bill. The X-ray powder diffraction measurement was performed on a Stoe STA-DI P transmission diffractometer, equipped with a primary Ge (111) monochromator and a linear position sensitive detector. The wavelength used was Mo K$_{\alpha 1}$: 0.7093 Å. Full powder patterns were taken from 2 to 20° 2θ in steps of 0.01° 2θ. Data were collected at room temperature.

X-ray Crystallographic Data Collection and Refinement of the Structures. A colorless single crystal of **1**, black crystals of **4**, **5**, and **6**·0.5 hexane, and a brown crystal of **7** were coated with perfluoropolyether, picked up with nylon loops, and were immediately mounted in the nitrogen cold stream of the diffractometer to prevent loss of solvent. A Bruker-Nonius Kappa-CCD diffractometer was used for crystals of **4**. Compounds **1**, **5**, **6**·0.5 hexane, and **7** were measured on a Bruker APEX II diffractometer. Diffractometers were equipped with a Mo-target rotating-anode X-ray source and a graphite monochromator (Mo−Kα, λ = 0.71073 Å). Final cell constants were obtained from least-squares fits of setting angles of several thousand strong reflections. Intensity data were corrected for absorption using intensities of redundant reflections using SADABS.[21] The structures were readily solved by Patterson methods and subsequent difference Fourier techniques. The Bruker ShelXTL[22] software package was used for solution, refinement, and artwork of the structures. All non-hydrogen atoms were anisotropically refined, and hydrogen atoms were placed at calculated positions and refined as riding atoms with isotropic displacement parameters, except for the protons of the bridging OH-groups in crystals of **4**, which were located from the difference map for both crystallographically independent cations. A PF$_6^-$ anion in compound **4** was found to be disordered over two positions. A restrained split atom model was refined giving an occupation ratio of 0.88:0.12. Anisotropic displacement parameters of corresponding disordered atoms were restrained to be equal using EADP. P−F bond distances in the minor component were restrained to be equal within errors applying the SAME instruction of ShelXL97.

Density Functional Theory (DFT) Calculations. All DFT calculations were performed with the ORCA program package.[23] The geometry optimizations of the complexes were performed at the B3LYP[24−26] level of DFT, except for compounds **5**, **6**, and **7**, where geometry optimization at the BP86[24,27,28] level of DFT resulted in more accurate bond distances, by comparison to the experimental values. Single-point calculations on the optimized geometries were carried out using the B3LYP functional. This hybrid functional often gives better results for transition metal compounds than pure gradient-corrected functionals, especially with regard to metal−ligand covalency.[29] The all-electron Gaussian basis sets were those developed by the Ahlrichs group.[30,31] Triple-ζ quality basis sets TZV(P) with one set of polarization functions on the metals and on the atoms directly coordinated to the metal center were used.[30] For the carbon and hydrogen atoms, slightly smaller polarized split-valence SV(P) basis sets were used, that were of double-ζ quality in the valence region and contained

(21) *SADABS*, Vers. 2008/1; Bruker AXS Inc.: Madison, WI, 2003.
(22) *ShelXTL*, 6.14; Bruker AXS Inc.: Madison, WI, 2003.
(23) Neese, F. In *An ab initio, DFT and Semiempirical Electronic Structure Package*, Version 2.7, Revision 0; Institut für Physikalische und Theoretische Chemie, Universität Bonn: Bonn, Germany, 2009.
(24) Becke, A. D. *J. Chem. Phys.* **1986**, *84*, 4524.
(25) Becke, A. D. *J. Chem. Phys.* **1993**, *98*, 5648.
(26) Lee, C. T.; Yang, W. T.; Parr, R. G. *Phys. Rev. B* **1988**, *37*, 785.
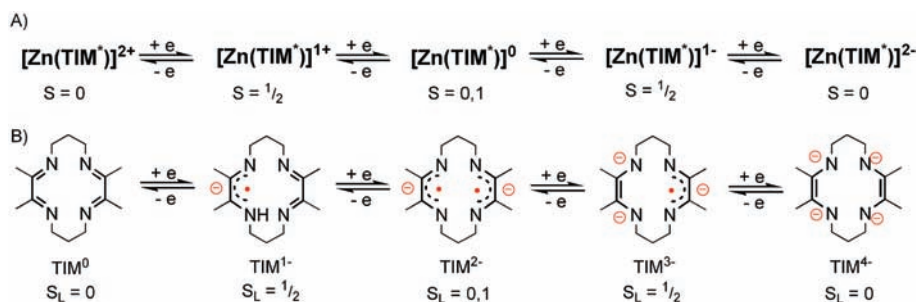(27) Perdew, J. P.; Yue, W. *Phys. Rev. B* **1986**, *33*, 8800.
(28) Perdew, J. P. *Phys. Rev. B* **1986**, *33*, 8822.
(29) Neese, F.; Solomon, E. I. In *Magnetism: From Molecules to Materials*; Miller, J. S., Drillon, M., Eds.; Wiley: New York, 2002; Vol. *4*, p 345.
(30) Schäfer, A.; Huber, C.; Ahlrichs, R. *J. Chem. Phys.* **1994**, *100*, 5829.
(31) Schäfer, A.; Horn, H.; Ahlrichs, R. *J. Chem. Phys.* **1992**, *97*, 2571.

Scheme 3

a polarizing set of d-functions on the non-hydrogen atoms.[31] Auxiliary basis sets used to expand the electron density in the resolution-of-the-identity (RI) approach were chosen,[32,33] where applicable, to match the orbital basis. The SCF calculations were tightly converged (1×10^{-8} E_h in energy, 1×10^{-7} E_h in the density change, and 1×10^{-7} in maximum element of the DIIS error vector). The geometry optimizations for all complexes were carried out in redundant internal coordinates without imposing symmetry constraints. In all cases the geometries were considered converged after the energy change was less than 5×10^{-6} E_h, the gradient norm and maximum gradient element were smaller than 1×10^{-4} E_h Bohr^{-1} and 3×10^{-4} E_h Bohr^{-1}, respectively, and the root-mean square and maximum displacements of all atoms were smaller than 2×10^{-3} Bohr and 4×10^{-3} Bohr, respectively. Computational results are described by the broken-symmetry (BS) approach.[34,35] Since several broken symmetry solutions to the spin-unrestricted Kohn−Sham equations may be obtained, the general notation BS(m,n)[36] has been adopted, where $m(n)$ denotes the number of spin-up (spin-down) electrons at the two interacting fragments. Canonical and corresponding orbitals[37] were generated with the program Molekel.[38] Non-relativistic single-point calculations on the optimized geometry were carried out to predict Mössbauer spectral parameters (isomer shifts and quadrupole splittings). These calculations employed the CP(PPP) basis set for iron.[39] The Mössbauer isomer shifts were calculated from the computed electron densities at the iron centers as previously described.[40a]

We are aware of the fact that DFT does not allow for rigorous handling of open-shell states since the total spin is not defined. For cases with the maximum number of unpaired electrons one can assume that the calculated state approaches the proper spin eigenstate, except for some possible small spin contamination. However, for an open-shell singlet, and also for other similar states where many multiplets are possible for a given open-shell configuration, the DFT solution is necessarily a mixture of multiplets.[40b,c]

Nevertheless, we use DFT calculations here to explore the basic electronic structure of a number of open-shell compounds, in particular, to explain their spectroscopic properties. However, in all cases the spin ground state of a given molecule was experimentally determined. We do not attempt to infer details of the spin coupling scheme from the present computational results.

(32) Eichkorn, K.; Weigend, F.; Treutler, O.; Ahlrichs, R. *Chem. Phys. Lett.* **1995**, *240*, 283.

(33) Eichkorn, K.; Treutler, O.; Öhm, H.; Häser, M.; Ahlrichs, R. *Chem. Phys. Lett.* **1995**, *242*, 652.

(34) Ginsberg, A. P. *J. Am. Chem. Soc.* **1980**, *102*, 111.

(35) Noodleman, L.; Peng, C. Y.; Case, D. A.; Mouesca, J. M. *Coord. Chem. Rev.* **1995**, *144*, 199.

(36) Kirchner, B.; Wennmohs, F.; Ye, S.; Neese, F. *Curr. Opin. Chem. Biol.* **2007**, *11*, 134.

(37) Neese, F. *J. Phys. Chem. Solids* **2004**, *65*, 781.

(38) *Molekel*; http:\\\\www.cscs.ch/molkel/.

(39) Neese, F. *Inorg. Chim. Acta* **2002**, *337*, 181.

(40) (a) Sinnecker, S.; Slep, L. D.; Bill, E.; Neese, F. *Inorg. Chem.* **2005**, *44*, 2245. (b) Ziegler, T.; Rauk, A.; Baerends, E. *Theor. Chim. Acta* **1977**, *43*, 261. (c) Illas, F.; Moreira, I.; Bofill, J.; Filatov, M. *Theor. Chem. Acc.* **2006**, *116*, 587.
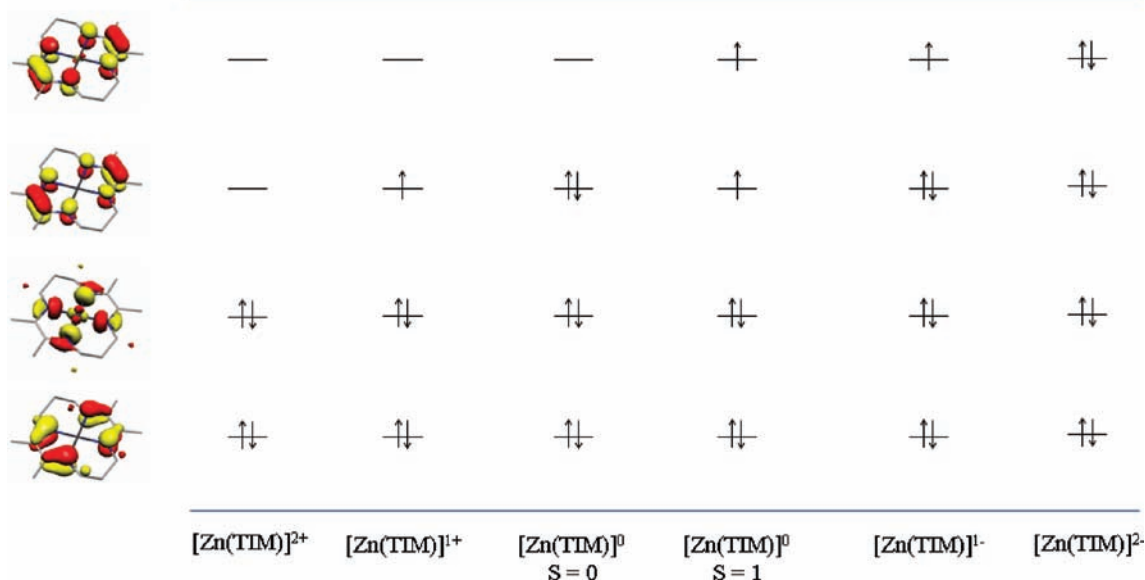
3. Results and Discussion

DFT Computational Studies on the Zn- and Fe-TIM* Redox Series. To simplify the structural analyses of M(TIM*) complexes, we have carried out DFT computational studies on a redox series of monomeric Zn- and Fe-coordinated TIM* species, as described below. The series, beginning with the fully oxidized dicationic [M(TIM*)]$^{2+}$ through the dianionic [M(TIM*)]$^{2-}$, disentangle the effect of the metal ion and ligand oxidation state on the electronic structure of metal-TIM* complexes.

[Zn(TIM*)]^n series. DFT computational studies were carried out, using the B3LYP functional, on each member of a 4e- redox series of monomeric Zn(TIM*) species shown in Scheme 3A. Geometry optimizations and electronic structure determinations were carried out for each species with ground states as defined in Scheme 3A.

The Zn series illustrates the nature of ligand-centered redox processes, virtually uncomplicated by the metal ion, which in all cases comprises a Zn(II) ion (d^{10}, $S_{Zn} = 0$). The low energy of the Zn d-orbitals precludes significant overlap with the ligand orbitals; five doubly occupied 3d metal orbitals were identified in each case that lie far below the ligand centered valence orbitals in energy. The increasing negative charge across the [Zn(TIM*)]^n series, thus, reflects the consecutive one electron reduction of the TIM* macrocycle (Scheme 3B), as borne out by the DFT-derived molecular orbital (MO) diagrams for the Zn(TIM*) series (Figure 1). Each reduction leads to the successive occupancy of the ligand imine π^* orbitals.

A clear trend in the calculated α-diimine $C_{im}-C_{im}$ and $C_{im}-N_{im}$ bond distances is manifest across the [Zn(TIM*)]^n redox series: an increase in the $C_{im}-N_{im}$ bonds lengths is observed with each successive reduction, corresponding to a decrease of the $C_{im}-C_{im}$ bond distance (Figure 2). The trend is as expected in proceeding from the fully oxidized [Zn^{II}(TIM^0)]$^{2+}$ to the fully reduced [Zn^{II}(TIM^{4-})]$^{2-}$. The dicationic species, [Zn^{II}(TIM^0)]$^{2+}$, consists of the neutral TIM^0, with four $C_{im}-N_{im}$ double bonds and two $C_{im}-C_{im}$ single bonds. The DFT derived MO diagram for the dianionic species, [Zn^{II}(TIM^{4-})]$^{2-}$, represents the fully reduced macrocyle, TIM^{4-}. The two doubly occupied ligand π^* orbitals are antibonding with respect to the $C_{im}-N_{im}$ bonds and bonding with respect to the $C_{im}-C_{im}$ bonds, concurrent with the altered bond distances, yielding four $C_{im}-N_{im}$ single bonds and two $C_{im}=C_{im}$ double bonds (Scheme 3B). The calculated structures of the monocationic [Zn^{2+}(TIM^{1-})]$^{1+}$ and the monoanionic [Zn^{2+}(TIM^{3-})]$^{1-}$ complexes imply that the unpaired electron in each molecule is delocalized over both diimine units of the TIM^{1-} or TIM^{3-} ligand, since in both structures the two $C_{im}-N_{im}$

Figure 1. DFT derived (B3LYP) qualitative molecular orbital scheme for the $[Zn(TIM)]^n$ redox series. The ligand centered frontier orbitals are depicted; Zn d-orbitals lie well below in energy.
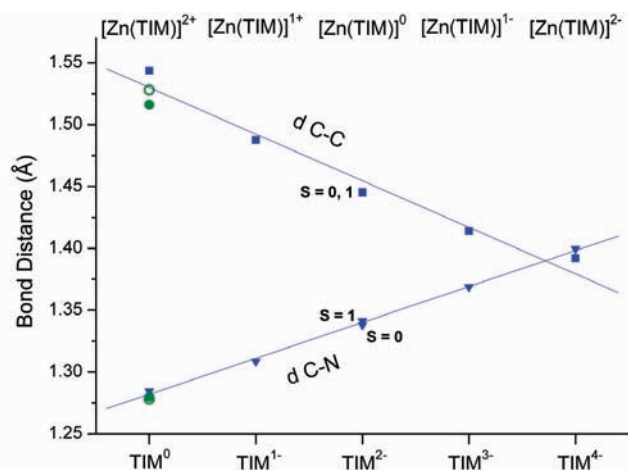

Figure 2. DFT derived TIM α-diimine bond distances across the 4e-$[Zn(TIM)]^n$ redox series; (blue solid squares) α-diimine C−C bond distances, (blue solid triangles) α-diimine C−N bond DFT calculated (green open circles) and crystallographically determined (green solid circles) α-diimine C−C and C−N bond distances for $[Zn(TIM)Cl]^{1+}$ also shown for comparison.

bond distances and the two $C_{im}-N_{im}$ bond distances are equivalent.

Both the $S = 0$ and $S = 1$ spin states of the neutral $[Zn^{II}(TIM^{2-})]^0$ species were examined. The bond distances of the two structures are nearly identical, since the nature of the occupied diimine π* orbitals is identical with respect to the C−N and C−C bonding character. The triplet diradical and closed-shell singlet species also are nearly degenerate in energy; the calculated energy difference between the two states was found to be a mere 3.8 kcal/mol in favor of a triplet ground state. The near degeneracy contrasts with other square planar metal complexes containing ligand diradicals, where strong antiferromagnetic interactions between the two ligand-centered spins arise via

(41) Blanchard, S.; Neese, F.; Bothe, E.; Bill, E.; Weyhermüller, T.; Wieghardt, K. *Inorg. Chem.* **2005**, *44*, 3636.

coupling through the $S = 0$ metal center, in favor of a diamagnetic ground state.[41]

The experimentally determined bond distances obtained from the crystal structure of the $[Zn^{II}(TIM^0)(Cl)]^+$ complex (**1**) (vide infra) provide a reference for the calculated values, and are in close agreement with the DFT-derived bond lengths for the $[Zn^{II}(TIM^0)]^{2+}$ dication (Table 1). The slight discrepancy is attributed to the presence of the fifth ligand (the Cl^- ion) in **1**. Indeed, the bond distances derived from computational studies on the $[Zn^{II}(TIM^0)Cl]^+$ moiety ($C_{im}-C_{im}$(avg) = 1.528 Å; $C_{im}-N_{im}$(avg) = 1.278 Å) are well matched with the experimentally determined values ($C_{im}-C_{im}$(avg) = 1.516(2) Å; $C_{im}-N_{im}$(avg) = 1.278(1) Å).
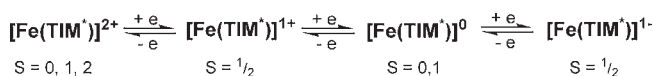
$[Fe(TIM*)]^n$ Series. An analogous redox series of Fe-(TIM*) species, namely, $[Fe(TIM*)]^{2+} \rightarrow [Fe(TIM*)]^{1-}$ (Scheme 4), also was investigated using DFT methods.

As illustrated in Figure 4, the Fe(TIM*) series is considerably more complex than the Zn(TIM*) series. The oxidation state of the ligand strongly influences the spin state at the iron ion and reduction of the macrocycle coincides with significant orbital rearrangements across the series. Both low-spin and intermediate spin Fe^{II} ions are observed. Yet despite the presence of the redox-active iron ion, reduction also appears to be ligand based rather than metal centered. Thus, the iron center remains divalent across the series; we have not found any evidence from computational studies to support an $[Fe^I(TIM*)]^n$ or an $[Fe^0(TIM*)]^n$ species. This would suggest that Busch's $[Fe(tetraeneN_4)]^+(OTf)$ (OTf = triflate anion) and $[Fe(tetraeneN_4)]^0$ complexes should be formulated as $[Fe^{2+}(tetraeneN_4^{1-})]^+$ rather than $[Fe^{1+}(tetraeneN_4^0)]^+$, and $[Fe^{2+}(tetraeneN_4^{2-})]^0$ rather than $[Fe^0(tetraeneN_4^0)]^0$. DFT results for $[Fe(TIM)(OTf)]$ demonstrate that the electronic structure is not perturbed by coordination of the anion (Supporting Information); the five coordinate triflate complex also consists of a divalent iron ion and an anionic (TIM^{1-}) ligand. Likewise, monomeric $[Fe^{2+}(tetraeneN_4^{2-})]^0$ provides a more accurate description of the reported $[Fe^0(tetraeneN_4)]$ species, regardless of the total spin state of the molecule.

Table 1. Select M(TIM*) Bond Lengths from DFT Calculations and Crystallographic Values

Complex	bond	[TIM]⁰ S = 0	[TIM]¹⁻ S = ½	[TIM]²⁻ S = 0	[TIM]²⁻ S = 1	[TIM]³⁻ S = ½	[TIM]⁺ S = 0
Calculated							
Zn series	C-N	1.285	1.309	1.338	1.341	1.369	1.3995
	C-C	1.544	1.489	1.446	1.445	1.414	1.392
Fe series	C-N	1.293	1.332	1.347	1.363	1.368	
	C-C	1.513	1.445	1.425	1.408	1.409	
[Zn(TIM)(Cl)]⁺	C-N	1.278					
	C-C	1.528					
[Fe(TIM)(MeCN)₂]²⁺	C-N	1.291					
	C-C	1.504					
Experimental							
[Zn(TIM)(Cl)]⁺(PF₆)	C-N	← 1.278(1) →					
	C-C	← 1.516(2) →					
[Fe(TIM)(MeCN)₂]²⁺(PF₆)₂	C-N	← 1.292(4) →					
	C-C	← 1.487(3) →					
[Fe(TIM)]₂	C-N			← 1.353(3) →			
	C-C			← 1.399(3) →			

Scheme 4

$$[\text{Fe(TIM}^*)]^{2+} \underset{-e}{\overset{+e}{\rightleftharpoons}} [\text{Fe(TIM}^*)]^{1+} \underset{-e}{\overset{+e}{\rightleftharpoons}} [\text{Fe(TIM}^*)]^{0} \underset{-e}{\overset{+e}{\rightleftharpoons}} [\text{Fe(TIM}^*)]^{1-}$$

S = 0, 1, 2   S = ½   S = 0,1   S = ½

However, a description as a dimer is conceivable, in light of the [Fe(TIM*)]₂ structure.[42]

The trend in the α-diimine $C_{im}-N_{im}$ and $C_{im}-C_{im}$ bond distances (Figure 3) parallels that of the Zn series. However, the values for the $C_{im}-C_{im}$ bond distances all are shorter than the analogous bond lengths in the Zn series ($\Delta d \sim 0.03$ Å), while the C−N bond distances all are slightly longer ($\Delta d \sim 0.01$ Å). This effect is a consequence of greater overlap of the Fe d orbitals with the ligand π^* orbitals, giving rise to enhanced π-backbonding effects. The ligand π^* orbitals possess greater electron density than in the corresponding orbitals of the Zn(TIM*) species stemming from the increased covalency of the Fe−N versus Zn−N bonds. The largest variation in the α-diimine bond lengths occurs with the reduction of [Fe(TIM*)]²⁺ to [Fe(TIM*)]¹⁺, which corresponds to a change in the metal spin state from low-spin ($S_{Fe} = 0$) to intermediate-spin ($S_{Fe} = 1$). The diimine bond distances also are dependent on the total spin state of the molecule, as shown for the singlet ($S_T = 0$) and triplet ($S_T = 1$) states of the [Fe^{II}(TIM⁰)]²⁺ and [Fe^{II}(TIM²⁻)]⁰ species. The triplet state of [Fe^{II}(TIM⁰)]²⁺ was found to be 34 kcal/mol lower in energy than the singlet state, as expected for a four-coordinate square planar molecule containing a divalent Fe ion (d⁶, $S_{Fe} = 1$). The triplet and singlet states of [Fe^{II}(TIM²⁻)]⁰, however, are again nearly isoenergetic ($\Delta E(S_T = 0 - S_T = 1)$: 3.6 kcal/mol). Given the near-degeneracy of the two structures, one might expect the two-electron reduced [Fe(TIM*)]⁰ to be particularly reactive. Formation of the [Fe(TIM*)]₂ dimer might in fact proceed via a pathway involving the neutral, [Fe(TIM*)]⁰, triplet diradical complex, which consists of a singly occupied d_{z^2} orbital and is thus primed for the formation of the Fe−Fe bond. Noteworthy are the $C_{im}-C_{im}$ and
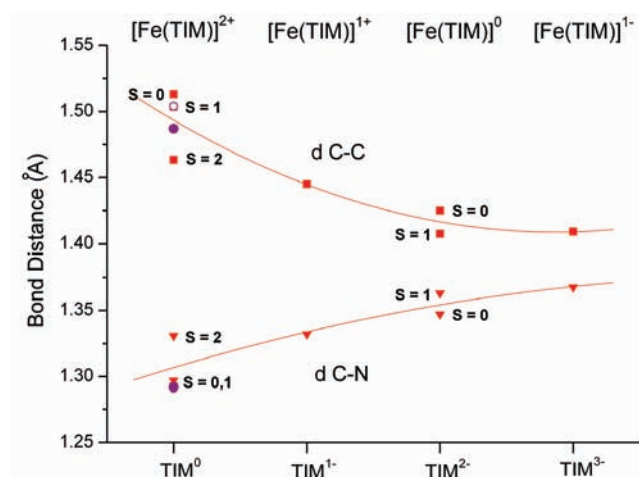

Figure 3. DFT derived TIM α-diimine bond distances across the 3e-[Fe(TIM)]ⁿ redox series; (red solid squares) α-diimine C−C bond distances, (red solid triangles) α-diimine C−N bond distances. DFT calculated (purple open circles) and crystallographically determined (purple solid circles) α-diimine C−C and C−N bond distances for [Fe(TIM)(MeCN)₂]²⁺ also shown for comparison.

$C_{im}-N_{im}$ distances in the calculated structure of [Fe(TIM*)]⁰, which indicate the presence of an Fe^{II} ion and a TIM²⁻ ligand.

The experimental bond distances determined for [Fe(TIM)(MeCN)₂]²⁺(PF₆)₂ ($C_{im}-C_{im}$(avg) = 1.487(3) Å; $C_{im}-N_{im}$(avg) = 1.292(4) Å)[19] provide reference values for the Fe series. The crystallographic values are in close agreement with the calculated α-diimine bond distances for the singlet [Fe^{II}(TIM⁰)]²⁺ species, and nearly identical to the geometry optimized values for the [Fe^{II}(TIM⁰)(MeCN)₂]²⁺ structure ($C_{im}-C_{im}$(avg) = 1.504 Å; $C_{im}-N_{im}$(avg) = 1.291 Å). The values for the C−C and C−N bond distances of the [Fe(TIM*)]₂ dimer lie precisely in between the value calculated for the [Fe²⁺(TIM²⁻)]⁰ and [Fe²⁺(TIM³⁻)]¹⁻ species (Table 1), in further support of the presence of a mixed valent TIM²·⁵⁻ ligand. The explicit trend in the diimine bond lengths illustrates the value of crystallographic data in establishing the ligand oxidation state in metal-coordinated α-diimine macrocyclic complexes. However, the series also highlights scenarios where

---

(42) The Mössbauer parameters of Busch's two-electron reduced complex are very similar to those reported for [Fe(TIM*)]₂ ($\delta = 0.13$ mm/s, $\Delta E_Q = 2.23$ mm/s); Scarborough, C. C., Wieghardt, K., unpublished.
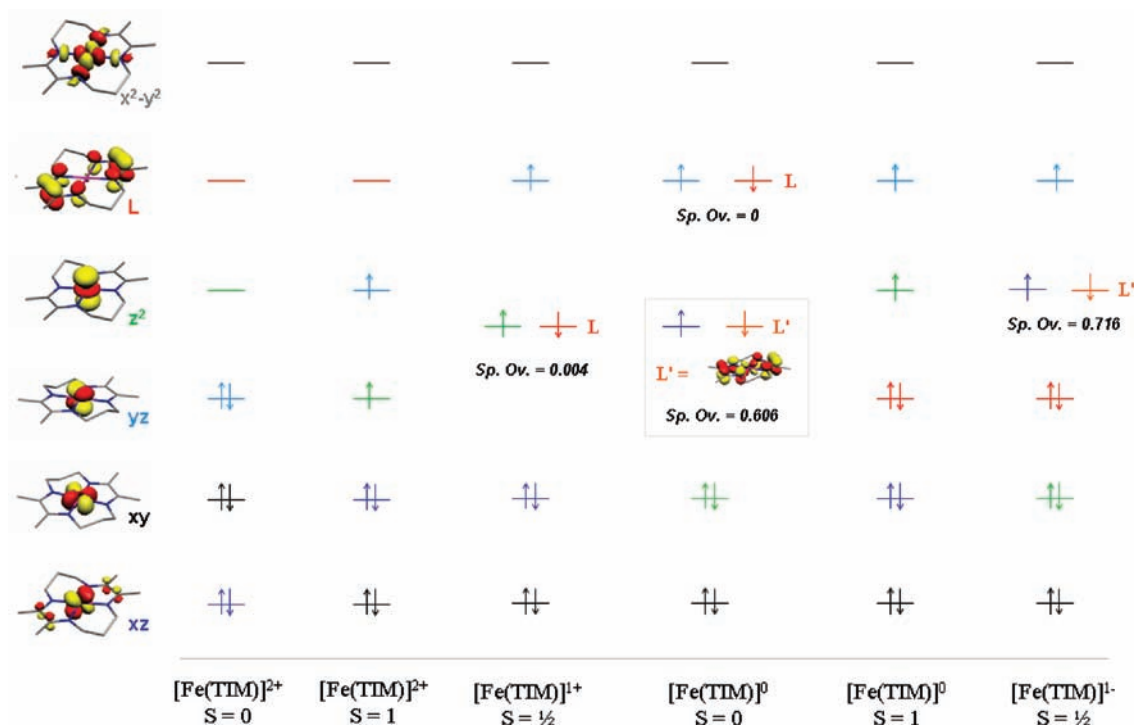
The figure shows a molecular orbital scheme with orbital rows labeled (top to bottom): x^2-y^2, L, z^2, yz, xy, xz. Annotations include "Sp. Ov. = 0", "Sp. Ov. = 0.004", "Sp. Ov. = 0.606", "Sp. Ov. = 0.716", and "L' =".

Column labels:

$[Fe(TIM)]^{2+}$ $S = 0$	$[Fe(TIM)]^{2+}$ $S = 1$	$[Fe(TIM)]^{1+}$ $S = \frac{1}{2}$	$[Fe(TIM)]^{0}$ $S = 0$	$[Fe(TIM)]^{0}$ $S = 1$	$[Fe(TIM)]^{1-}$ $S = \frac{1}{2}$

Figure 4. DFT derived (B3LYP) qualitative molecular orbital scheme for the $[Fe(TIM)]^{n}$ redox series. Sp. Ov. = DFT derived spatial overlap.

precise electronic structure assignments become more difficult. The calculated α-diimine bond distances for the $[Fe(TIM^*)]^{0}$ triplet diradical are comparable to the values obtained for the monoanionic $[Fe(TIM^*)]^{1-}$. Therefore, crystallographic evidence alone would be insufficient to distinguish between the trianionic TIM^{3-} and the dianionic TIM^{2-} ligand.

Reactivity. Synthesis and Characterization. Compound **1** was prepared according to the procedures described by Jackels et al. for the synthesis of [Zn(MePhTIM)Cl]-PF₆ (MePhTIM = 2,9-dimethyl-3,10-diphenyl-1,4,8,11-tetra-azacyclo-tetradeca-1,3,8,10-tetraene).[20] The procedure entails the reductive transmetalation of [Cu(TIM)]ZnCl₄; the latter complex, likewise, was prepared according to the published methods for the MePhTIM analogue.[43] ¹H NMR illustrates that compound **1** is diamagnetic, as expected upon coordination of the redox-inert Zn ion to the neutral TIM^{0} ligand. The cyclic voltammogram (CV) in acetonitrile exhibits a reversible one-electron reduction at −1.66 V versus ferrocenium/ferrocene (Fc⁺/Fc) (Supporting Information). This process is assigned as a ligand-centered reduction. The isolation of reduced Zn(TIM*) products (i.e., $[Zn^{II}(TIM^{1-})]^{+}$ or $[Zn^{II}(TIM^{2-})]^{0}$) proved unsuccessful.

The dication of octahedral compound **2**, which consists of the neutral TIM^{0} ligand, a low spin ferrous ion, and two acetonitrile ligands in the trans-position, was the initial choice of starting reagent to access and examine further redox states of Fe(TIM*) complexes. The CV of **2** in acetonitrile (0.2 M TBAPF₆, 25 °C; Figure 5) exhibits a fully reversible one-electron oxidative wave at +0.59 V versus Fc⁺/Fc, as well as two closely spaced, one-electron reductive processes at $E_{1/2}$ = −1.13 V and −1.60 V. These potentials agree nicely with the values reported for the reduction of Busch's $[Fe^{II}(tetraeneN_4^{0})(MeCN)_2]^{2+}(OTf)_2$ complex.[14] Controlled potential coulometry of a solution

of **2** (MeCN, ∼ −1.4 vs Fc⁺/Fc) cleanly generates the one-electron reduced product; the electronic spectrum coincides with new bands in the region from 600−800 nm (λ_{max} = 640 nm) and a blue-shift of the absorption band at 552 nm that correspond to the starting complex (Figure 5, inset). The first reduction is clearly reversible, given that the CV is reproducible subsequent to coulometry, and reoxidation of the sample restores the original absorption spectrum of **2**. The anisotropic EPR spectrum of the electrochemically generated one-electron reduced product affords g values of 2.50, 2.07, and 2.0 (Supporting Information). The values again are in close agreement with those reported for the EPR spectrum of the $[Fe(tetraeneN_4^*)]^{+}$ species (g = 2.302, 2.074, 2.006), which was assigned to an Fe^{I} complex.[14] However, the EPR values also are entirely consistent with an intermediate spin Fe^{II} center antiferromagnetically coupled to the ligand π-radical anion ((TIM^{1-}) or (tetraeneN₄$^{1-}$)), which would signify ligand centered reduction. The second reductive process observed in the CV of **2** is irreversible, and its electrochemical generation proved unsuccessful.

The one-electron reduced product could not be obtained synthetically. As reported previously, chemical reduction of [Fe(TIM*)(MeCN)₂](PF₆)₂ using Na/Hg correspond to the two electron reduction of each Fe(TIM*) unit and yields the dimeric complex, [Fe(TIM*)]₂ (**3**); no additional products, such as monomeric intermediates preceding dimer formation, were observed. The triplet ground state and the weak metal−metal bond of [Fe(TIM*)]₂ suggested to us that compound **3** should be highly reactive toward small molecules. Indeed, the Fe−Fe dimer, composed of two reduced TIM ligands ([Fe$^{2.5}$(TIM$^{-2.5}$)]₂), provides an ideal route to further Fe(TIM*) complexes in various oxidation states, via the reaction with dioxygen, iodine, and phosphines (Scheme 5).

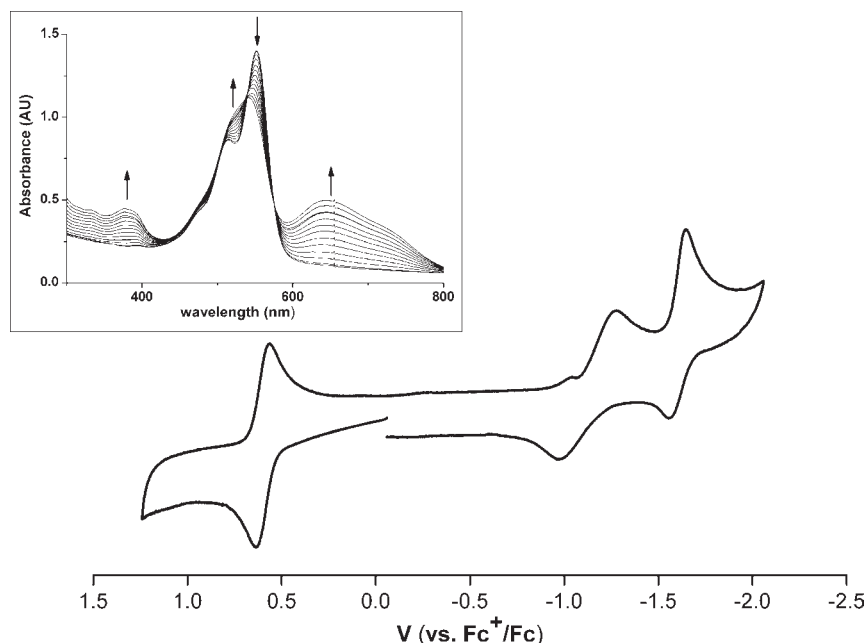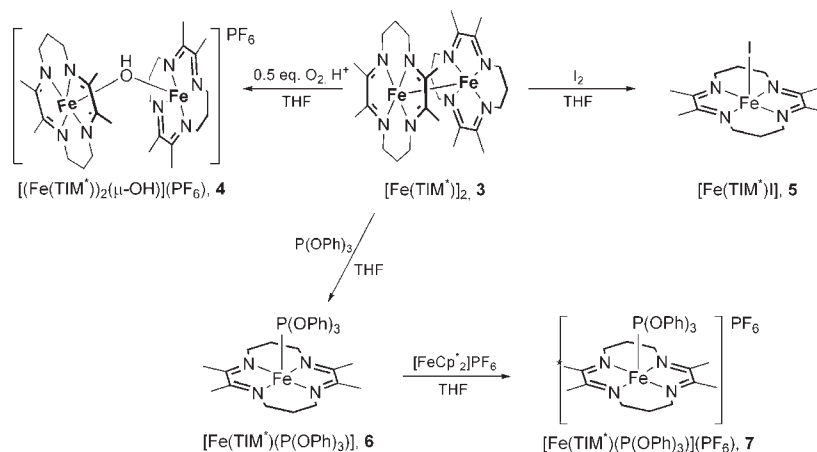(43) Coltrain, B. K.; Jackels, S. C. *Inorg. Chem.* **1981**, *20*, 2032.

Figure 5. Cyclic voltammogram of **2** in acetonitrile, 0.2 M TBAPF$_6$, 25 °C, 100 mV/s. Inset: Absorption spectrum of controlled potential coulometry of **2** (-1.4 V vs Fc$^+$/Fc) to generate the one-electron reduced species.

Scheme 5. Synthesis of Compounds **4**–**7** from [Fe(TIM*)]$_2$ (**3**)^a

^{a} Ligands have been drawn to more clearly describe the coordination geometry, and should not be taken as indicative of the the ligand oxidation state or electronic structure of these compounds (i.e. the TIM ligand in **1**–**7** is **NOT** in the fully oxidized TIM^0 form as depicted).

The reaction of [Fe(TIM*)]$_2$ with dioxygen, in the presence of a proton source (water), leads to the formation of the binuclear, hydroxo-bridged compound, [{Fe-(TIM*)}$_2$(μ-OH)](PF$_6$) (**4**).[44] The [{Fe(TIM*)}$_2$(μ-OH)]$^+$ cation denotes a two-electron oxidation of **3** by O$_2$. A color change of the solution from blue to violet-purple is observed during the reaction of [Fe(TIM)]$_2$ with air, correspondent with a blue shift in the absorption band of **3** at 578 nm, to 511 nm. Compound **4** is diamagnetic below 50 K, as established from magnetic susceptibility measurements (2–300 K, 1 T) (Figure 6). The best fit of

the data, assuming two independent spins of $S = 1/2$ ($H = -2JS_1S_2$; $S_1 = S_2 = 1/2$), yields a moderately large J value ($J = -92.5$ cm^{-1}) because of antiferromagnetic coupling of the two Fe(TIM*) units. The rise in μ_{eff} values from 50–300 K is indicative of an energetically low-lying paramagnetic excited state for this compound ($S_T = 1$).

Compound **5**, the neutral, five-coordinate compound, [Fe(TIM*)I], is readily generated from the reaction of [Fe(TIM*)]$_2$ with 1 equiv of iodine. Each [Fe(TIM*)] unit of **3** is oxidized by one electron, concomitant with coordination of the halide to the Fe center. The doublet ground state ($S_T = 1/2$) of the iodo-complex was confirmed by magnetic susceptibility measurements (Supporting Information), which also indicate substantial intermolecular interactions in the solid state (Weiss constant, $\theta = -21.9$ K). The crystalline solid of **5** is dark purple and exhibits absorption bands at 540 and 672 nm in the electronic spectrum.

---

(44) Dioxygen is added to the [Fe(TIM)]$_2$ solutions by injecting an appropriate volume of air, and the necessary protons were obtained from moisture present; this method, as detailed in the Experimental Section, proved to be the cleanest and most consistent route for the synthesis of [{Fe(TIM*)}$_2$(μ-OH)](PF$_6$). Attempts to use other proton sources, including pyridinium-hexafluorophosphate, were unsuccessful.
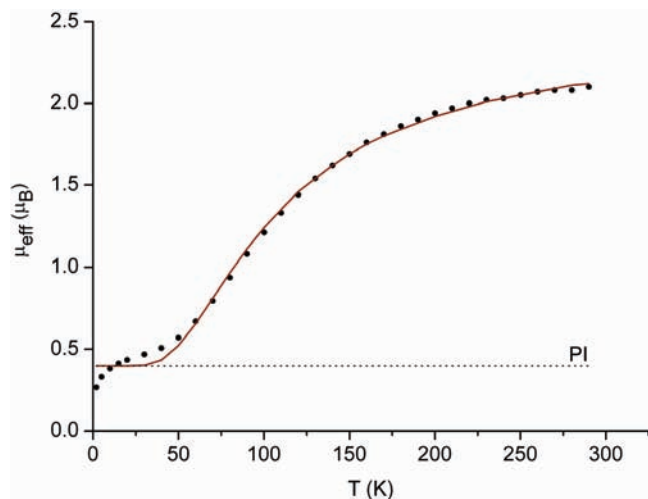
Figure 6. Magnetic susceptibility data (1 T, 2−300 K) for **4**; experimental = solid dots, simulation = solid line. Simulation with $S_1 = S_2 = 1/2$, $g_1 = g_2 = 2.0$, $J = -92.5\,\text{cm}^{-1}$, TIP = $1005 \times 1\text{e}^{-6}$ emu. The simulation includes a small percentage (0.4%) of high spin ($S = 2.5$) impurity, shown as dashed line (PI), which accounts for the values of $u_{eff} > 0$ from 2−40 K.

These features resemble the charge transfer (CT) bands observed in the spectrum of a structurally related iodo-Fe(III)-diiminosemiquinonate, which are characteristic of diimine ligand diradicals.[45]

The reaction of **3** with triphenylphosphite, likewise, breaks the Fe−Fe bond and generates the neutral, five-coordinate, [Fe(TIM*)(P(OPh)$_3$)] complex (**6**). Formally, this reaction does not represent a redox reaction, rather it is an addition of 2 equiv of the phosphite to 1 equiv of the dimer, **3**. The ^{1}H NMR illustrates that compound **6** is diamagnetic. The CV of **6** (THF) exhibits a single reversible one-electron oxidative process at −1.2 V versus Fc$^+$/Fc (Supporting Information). On the basis of this potential, bis(pentamethylcyclopentadienyl)iron hexafluorophosphate ([FeCp*$_2$]PF$_6$) was chosen as the oxidative reagent to generate the cationic [Fe(TIM*)(P(OPh)$_3$)]$^+$ complex (**7**). As for compound **5**, the oxidized phosphite complex has a doublet ground state (Supporting Information) and exhibits intense absorption bands in the 500−700 nm region of the electronic spectrum, giving rise to the purple color of solutions of **7**.

Solid State Structures. The solid state structures of compounds **1** and **4**−**7** are shown in Figures 7−9. The crystallographic data are listed in Table 2. The crystallographic data for compounds **2** and **3** has been described elsewhere.[19]

The Zn^{II}(TIM^0) complex, **1**, and the monomeric Fe(TIM*) complexes **5**−**7**, all are five-coordinate square pyramidal. The Zn ion in **1** is displaced significantly (0.83 Å) from the N$_4$-macrocyclic cavity, while in the iron compounds, the proximity of the metal to the N$_4$ plane is much closer (0.4−0.47 Å). In all structures, except **7**, the TIM ligand adopts a saddle-like structure, the two diimine units pointing downward, and the two methylene groups of the propyl backbones directed upward along the metal-axial bond. In the cationic [Fe(TIM*)(P(OPh)$_3$)]$^{2+}$ complex (**7**), these methylene groups adopt a trans configuration.
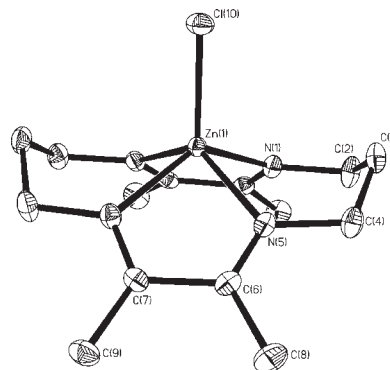

Figure 7. Thermal ellipsoid representation (50%) of **1**.
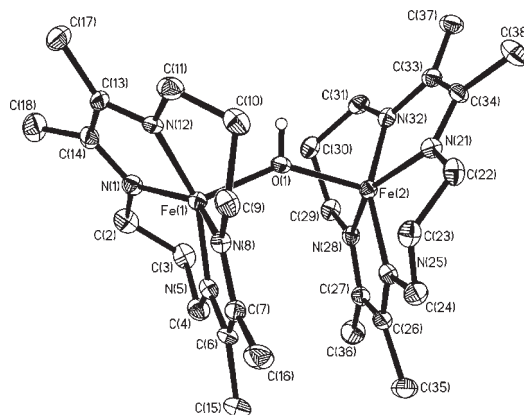

Figure 8. Thermal ellipsoid representation (50%) of **4**.

Of note are the Fe−P distances of compounds **6** and **7**: the Fe−P bond length of the cationic [Fe(TIM*)(P(OPh)$_3$)]$^+$ is significantly longer (2.181(1) Å) than the corresponding axial bond of the neutral [Fe(TIM*)(P(OPh)$_3$)] molecule (Fe−P = 2.085(1) Å). The same trend was previously described in an analogous five-coordinate iron phosphine complex coordinated by α-diimine ligands.[45] The shorter Fe−P bond of the neutral versus the cationic complex was attributed to the better π-backbonding ability of a ferrous versus ferric ion.

The hydroxo-bridged binuclear iron complex, **4**, has a "butterfly"-like structure: the Fe−O−Fe angle is 143°, enforcing the V-shape with respect to the two macrocyclic N$_4$-planes. Two conformers of **4** are observed within the unit cell, which differ slightly in the twist angle between the two Fe(TIM*) units about the hydroxo group. Each Fe center is square pyramidal and displaced by 0.46−0.47 Å from its N$_4$-cavity plane. The Fe−O bond distances (1.977(3) Å and 1.994(3) Å) are in accord with the range of values observed for (μ-hydroxo)diiron(III) complexes.[46−48] Compound **4** closely resembles the reported structure of a (μ-hydroxo)bis(octaethylporphyrinato)iron(III) complex,[46] and affords only the third example of a hydroxo-bridged diiron complex lacking additional supporting bridging ligands.[49]

(45) Chlopek, K.; Bill, E.; Weyhermüller, T.; Wieghardt, K. *Inorg. Chem.* **2005**, *44*, 7087.

(46) Scheidt, W. R.; Cheng, B.; Safo, M. K.; Cukiernik, F.; Marchon, J.-C.; Debrunner, P. G. *J. Am. Chem. Soc.* **1992**, *114*, 4420.

(47) Stamatatos, T. M.; Christou, A. G.; Jones, C. M.; O'Callaghan, B. J.; Abboud, K. A.; O'Brien, T. A.; Christou, G. *J. Am. Chem. Soc.* **2007**, *129*, 9840.

(48) Jullien, J.; Juhasz, G.; Dumas, E.; Mayer, C. R.; Marrot, J.; Riviere, E.; Bominaar, E. L.; Munck, E.; Secheresse, F. *Inorg. Chem.* **2006**, *45*, 6922.

(49) Evans, D. R.; Mathur, R. S.; Heerwegh, K.; Reed, C. A.; Xie, Z. *Angew. Chem., Int. Ed.* **1997**, *36*, 1335.
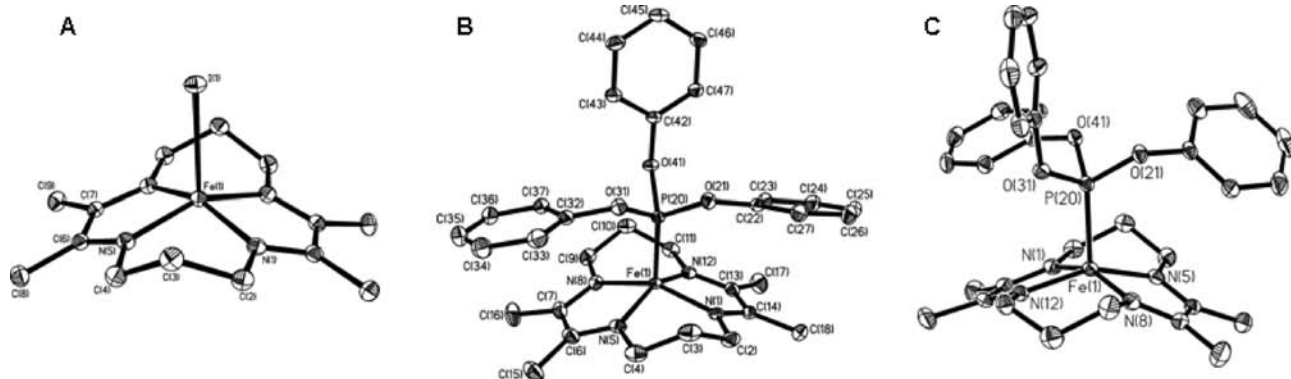
Figure 9. Thermal ellipsoid representation (50%) of compounds **5**−**7**.

Table 2. Crystallographic Data for **1**, **4**, **5**, **6**·0.5Hexane, and **7**

	1	**4**	**5**	**6**·0.5 hexane	**7**
chem. formula	$C_{14}H_{24}ClF_6N_4PZn$	$C_{28}H_{49}F_6Fe_2N_8OP$	$C_{14}H_{24}FeIN_4$	$C_{35}H_{46}FeN_4O_3P$	$C_{32}H_{39}FeN_4O_3P$
Fw	494.16	770.42	431.12	657.58	759.46
space group	$P4_32_12$, No. 96	$P2_1/c$, No. 14	$Pbcn$, No. 60	$P\bar{1}$, No. 2	$P2_1/c$, No. 14
a, Å	9.0688(6)	13.1409(8)	9.9374(8)	8.795(2)	13.572(2)
b, Å	9.0688(6)	13.7913(8)	14.8792(13)	9.128(2)	16.327(2)
c, Å	24.056(2)	37.013(3)	10.7044(9)	20.810(4)	15.444(2)
α, deg	90	90	90	89.791(4)	90
β, deg	90	91.606(3)	90	89.028(4)	109.529(2)
γ, deg	90	90	90	78.168(4)	90
V, Å	1978.4(2)	6705.2(8)	1582.8(2)	1635.0(6)	3225.6(6)
Z	4	8	4	2	4
T, K	100(2)	100(2)	100(2)	100(2)	100(2)
ρ calcd, g cm^{-3}	1.659	1.526	1.809	1.336	1.564
refl. collected/$2\Theta_{max}$	135983/70.00	85789/52.00	56015/72.96	45386/61.98	73290/55.00
unique refl./$I > 2\sigma(I)$	4365/4304	13148/9326	3812/2718	10322/8745	7412/5317
no. of params/restr.	126/0	873/23	94/0	402/0	437/0
λ, Å /$\mu(K\alpha)$, cm^{-1}	0.71073/15.19	0.71073/9.83	0.71073/29.00	0.71073/5.51	0.71073/6.43
R1^a/goodness of fit^b	0.0193/1.127	0.0528/1.016	0.0238/1.101	0.0388/1.082	0.0372/1.051
wR2^c ($I > 2\sigma$ (I))	0.0537	0.1082	0.0556	0.0936	0.0780
residual density, e Å^{-3}	+0.56/−0.34	+0.49/−0.60	+1.56/−0.56	+1.16/−0.54	+0.81/−0.52

^{a} Observation criterion: $I > 2\sigma(I)$. R1 $= \sum ||F_o| - |F_c||/\sum |F_o|$. ^{b} GoF $= \sum[w(F_o^2 - F_c^2)^2]/(n - p)]^{1/2}$ ^{c} wR2 $= [\sum w(F_o^2 - F_c^2)^2/\sum w(F_o^2)^2]^{1/2}$ where $w = 1/\sigma^2(F_o^2) + (aP)^2 + bP$, $P = (F_o^2 + 2F_c^2)/3$.

The crystallographically determined C−C and C−N α-diimine bond distances of the M(TIM*) structures, **1**−**7**, provide the first clues regarding the oxidation state of the ligand and, consequently, of the metal center. The bond distances can be compared readily to the DFT-derived ligand bond lengths of the monomeric [Zn(TIM*)]^n and [Fe(TIM*)]^n redox series. As discussed previously, the [Zn^{II}(TIM^0)Cl](PF$_6$) and [Fe^{II}(TIM^0)(MeCN)$_2$](PF$_6$)$_2$ complexes serve as benchmarks for the dicationic [Fe^{II}-(TIM^0)]$^{2+}$ unit, with a singlet ($S = 0$) ground state. The C$_{im}$−C$_{im}$ and C$_{im}$−N$_{im}$ bond distances of **1** and **2** (Table 1) are as expected for the C−C single bond and C=N double bonds of the fully oxidized TIM^0 ligand, containing four C=N double bonds.

Compound **6**, akin to the [Fe(TIM*)]$_2$ dimer, **3**, is composed of the neutral [Fe(TIM*)]^0 unit. The α-diimine C−C (1.407(2) Å) and C−N (1.342(2) Å) bond distances (Table 2) are similar to the values obtained for **3**. By comparison to the DFT-derived bond distances of the Fe(TIM*) series (Figure 3 and Table 1), the α-diimine bond lengths of **6** are in agreement with the calculated values for the dianionic TIM^{2-} ligand. The values are compatible with either a low spin or an intermediate spin Fe^{II} center.

The cationic [Fe(TIM*)]$^+$ unit of compounds **4**, **5**, and **7** is one-electron oxidized with respect to the [Fe(TIM*)]^0 moiety of the dimeric precursor compound (**3**). The α-diimine bond distances of compound **4** (C−C: 1.409(6), C−N: 1.339(6); Table 2) again are in accord with a TIM^{2-} diradical dianion, signifying the presence of two ferric ions. The bond distances of the two TIM^{2-} units are identical, ruling out a localized, mixed valent species of class I. On the basis of the structural data, a reasonable formulation of compound **4** is [{Fe^{3+}-(TIM^{2-})}$_2$(μ-OH)]$^+$. Likewise, the crystallographically determined α-diimine bond distances of **5** (C−C: 1.417(2), C−N: 1.338(2); Table 2) specify a dianionic TIM^{2-} ligand, and thus a ferric complex, represented by [Fe^{3+}(TIM^{2-})I].

The ligand bond distances of compound **7** deviate significantly from those of compounds **4** and **5** (Table 2). The C$_{im}$−C$_{im}$ distance at 1.442(4) Å is significantly longer, while the C$_{im}$−N$_{im}$ bond distance (1.317(3) Å) is substantially shorter than the corresponding bond lengths in the structures of compounds **4** and **5** (Table 3). The former values agree with the calculated distances for the monoanionic TIM^{1-} species. Consequently, the crystallographic data implies that the cationic unit of **7** consists of a ferrous ion coordinated by the TIM^{1-} radical anion ([Fe^{II}(TIM^{1-})(P(OPh)$_3$)]$^+$). Oxidation of the neutral

Table 3. Crystallographically Determined, Average Ligand α-Diimine and Axial Fe-L$_{ax}$ Bond Lengths for Compounds 4−7

compound	C$_{im}$−C$_{im}$ (avg), Å	C$_{im}$−N$_{im}$ (avg), Å	Fe−L$_{ax}$, Å
4	1.409(6)	1.339(6)	Fe$_A$−O: 1.977
			Fe$_B$−O: 1.994
5	1.417(2)	1.338(2)	L = I, 2.678
6	1.407(2)	1.342(2)	L = P, 2.085
7	1.442(4)	1.317(3)	L = P, 2.181

$[Fe^{II}(TIM^{2-})(P(OPh)_3)]$ (6) is thus ligand-centered. This contrasts with the synthesis of compounds 4 and 5, as both of the latter compounds appear to contain an Fe(III) center and TIM^{2-} ligands.

Spectroscopic Characterization. Mössbauer and EPR spectra (where applicable) were measured for compounds 4−7. In this series, only the [Fe(TIM*)(P(OPh)$_3$)] compound (6) consists of the neutral [Fe(TIM*)]^0 unit. The crystallographic data for the phosphite complex is consistent with an $[Fe^{2+}(TIM^{2-})(P(OPh)_3)]$ formulation (vide supra). Two electronic structures are viable for this diamagnetic compound: [(Fe↑↓)(TIM↓↑)], with a low-spin, $S_{Fe} = 0$, iron center and closed-shell, $S_L = 0$, ligand dianion; or [(Fe↑↑)(TIM↓↓)], composed of an intermediate spin ferrous ion, $S_{Fe} = 1$, and a triplet, $S_L = 1$, radical dianion. Antiferromagnetic interactions between the metal-centered and ligand-centered spins in the latter formulation give rise to the observed singlet, $S_T = 0$, ground state of the molecule. The zero-field Mössbauer spectrum of 6 at 80 K yields an isomer shift value of 0.14 mm/s and $\Delta E_Q = 1.99$ mm/s (Supporting Information). These values are similar to the Mössbauer parameters obtained for related, diamagnetic, 5-coordinate, Fe-phosphine complexes, containing ligand radical dianions.[45,50] However, the isomer shift and quadrupole splitting values do not unequivocally distinguish between the two possibilities afforded by the intermediate spin or low-spin Fe^{2+} configurations described above. The ambiguity regarding the metal spin state has likewise prevented a precise assignment of the electronic structure of the related Fe-phenylenediamine-phosphine, $[Fe^{II}(L_{N,N}^{2-})(PR_3)]$, and Fe-aminothiophenol-phosphite, $[Fe^{II}(L_{N,S}^{2-})(P(OPh)_3)]$ complexes.[45] However, among the examples of $[Fe^{II}(PR_3)(L^{\bullet\bullet^{2-}})]$ complexes, the low-spin iron configuration appears to be most prevalent.[50]

The remaining compounds in the synthetic Fe(TIM*) series, compounds 4, 5, and 7, all contain the monocationic [Fe(TIM*)]$^+$ unit. As stated above, the crystallographic data for [{Fe(TIM*)}$_2$(μ-OH)] (4) and [Fe(TIM*)I] (5) point to the presence of ferric ions coordinated by the dianionic, TIM^{2-}, ligands. The applied field Mössbauer spectrum of the μ-hydroxy dimer, 4, confirms the singlet ground state of the binuclear complex, and yields values of $\delta = 0.27$ mm/s, $\Delta E_Q = 1.69$ mm/s (4.2 K) for the isomer shift and quadrupole splitting (Supporting Information). The Mössbauer spectrum of 4 is unlike the spectra of analogous μ-hydroxo-bridged diiron(III) complexes (e.g., [(Fe(salen))$_2$(OH)]$^+$: $\delta = 0.49$ mm/s, $\Delta E_Q = -0.97$ mm/s;[46] [(Fe(octaethylporphinato))$_2$(OH)]$^+$: $\delta = 0.40$ mm/s, $\Delta E_Q = 1.13$ mm/s[48]), which all are characterized as high-spin ferric compounds. The isomer shift and quadrupole values of compound 4 are in line with either a
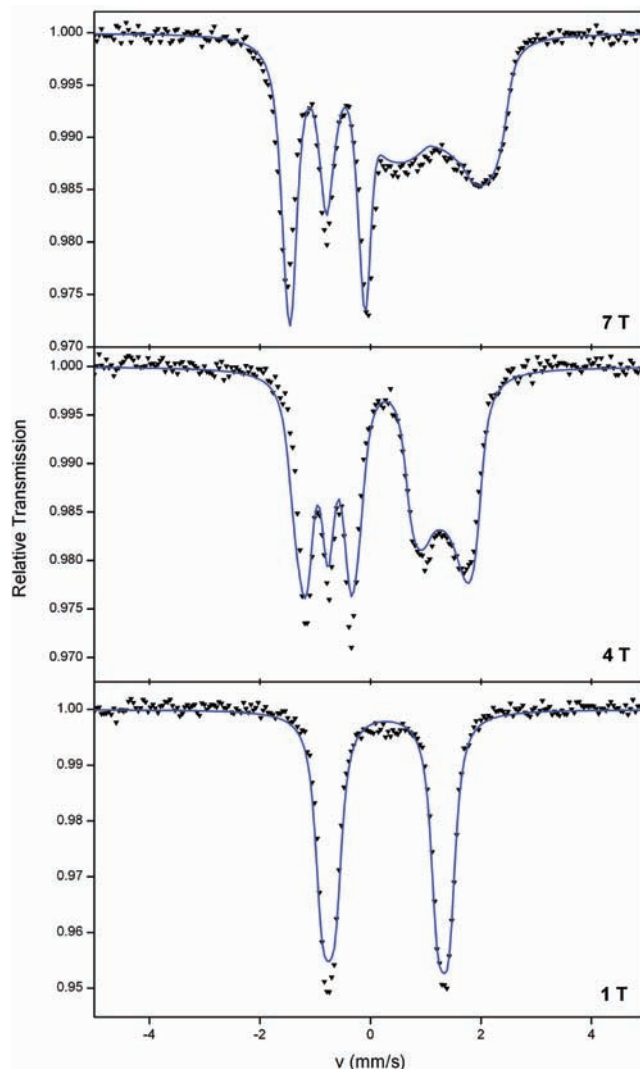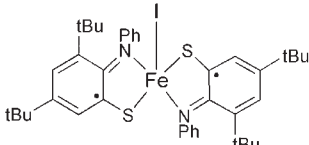
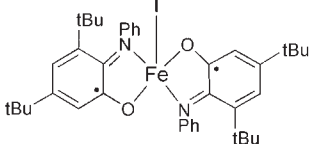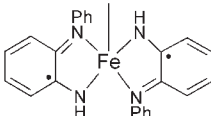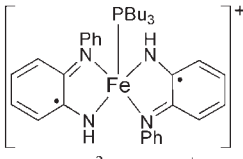(50) Ghosh, P.; Bill, E.; Weyhermüller, T.; Wieghardt, K. *J. Am. Chem. Soc.* **2003,** *125,* 3967.

Figure 10. Applied-field Mössbauer spectra of 5, measured at 4.2 K, 1−7 T. Experimental data shown as black triangles. Fit of the data (solid blue line), $S_T = 1/2$, affords: $\delta = 0.28$ mm/s, $\Delta E_Q = 2.07$ mm/s, $\eta = 0.1$, $g_x = g_y = g_z = 2.00$, [A/g$_N\beta_N$]: $A_{xx} = -6.03$ T, $A_{yy} = -32.44$ T, $A_{zz} = +0.50$ T. Isomer shift relative to α-Fe at 298 K.

low-spin or intermediate spin Fe^{III} configuration. The five-coordinate square pyramidal geometry at each Fe center favors an $S_{Fe} = 3/2$ spin state.

The values for the isomer shift and quadrupole splitting ($\delta = 0.28$ mm/s and $\Delta E_Q = 2.07$ mm/s) determined from the Mössbauer spectra of 5 are very similar to the data obtained for 4. The comparable values indicate an identical electronic structure with respect to the iron center of the shared monocationic [Fe(TIM*)]$^+$ unit. Applied-field Mössbauer spectroscopy (1−7 T, 4.2 K) provides further insight regarding the intrinsic spin state at the Fe center of the paramagnetic iodo-complex (Figure 10). The simulation of the magnetic spectra yields values for the hyperfine coupling constants, $\mathbf{A}(S_T = 1/2)/g_N\beta_N = (-6.03, -32.44, +0.50)$ T. The two large negative components and one smaller positive component of the hyperfine coupling tensor, denotes an intermediate spin ($S_{Fe} = 3/2$) ferric ion.[50] The A-tensor values can be converted to the intrinsic values for an intermediate spin iron center using spin projection techniques, and thus afford

Table 4. Mössbauer and EPR Values for **5** and **7**, and Related Compounds[a]

Compound	Mössbauer δ(mm/s), ΔE_Q (mm/s)	Magnetic Mössbauer $A/g_N\beta_N$ (T)	EPR values[b] g, A (10^{-4} cm^{-1}), P (10^{-4} cm^{-1})
[Fe(L$_{N,S}^{2-}$)$_2$I], Ref.45	δ = 0.15 ΔE_Q = 3.09	(S$_T$ = 1/2): -12.31, - 26.75, +1.0 (S$_{Fe}$ = 3/2): -7.38, -16.05, +0.6	g = 2.26, 2.12, 2.03 A = 3, 4, -19.1 P = -13.7, 8.1, 5.6 β = 11°
[Fe(L$_{N,O}^{2-}$)$_2$I], Ref. 51	δ = 0.24 ΔE_Q = 2.80	(S$_T$ = 1/2): (S$_{Fe}$ = 3/2): -12.4, - 20.3, +1.3	g = 2.34, 2.11, 2.05 A = 3, 15.5, 21 P = -13.3, 7.3, 6.0 β = 26°
[Fe(L$_{N,N}^{2-}$)$_2$I], Ref. 50	δ = 0.16 ΔE_Q = 2.90	(S$_T$ = 1/2): -9.49, - 28.32, +1.77 (S$_{Fe}$ = 3/2): -5.69, -16.99, +1.06	g = 2.28, 2.12, 2.03 A = 3, 4, -16 P = -19, 15, 4.0
5, [Fe(TIM*****)I]**	δ = 0.28 ΔE_Q = 2.07	(S$_T$ = 1/2): -6.03, - 32.44, +0.50 (S$_{Fe}$ = 3/2): -3.62, -19.47, +0.30	g = 2.376, 2.102, 2.012 A = 4, 11, -16 P = 6, -10, 4.0 β = 30°, γ = 90°
[Fe(L$_{N,N}^{2-}$)$_2$(PR$_3$)]$^+$, Ref. 45	δ = 0.05 ΔE_Q = 2.62	(S$_T$ = 1/2): -5.51, -22.76, +0.67 (S$_{Fe}$ = 3/2): -3.31, -13.66, +0.40	g = 2.28, 2.09, 2.01
7, [Fe(TIM*****)(P(OPh$_3$))]$^+$**	δ = 0.17 ΔE_Q = -0.35	(S$_T$ = 1/2): -0.43, +1.05, +0.20	g = 2.342, 2.073, 2.0198

[a] For all compounds, the Applied-Field Mössbauer was measured at 4.2 K and the EPR measured as frozen solutions, at 10 K. The EPR spectra of **5** and **7** were measured in THF. Further details can be found within the text or in the references indicated. [b] β and γ values refer to Euler angles that determine the rotation of the electric field gradient tensor with respect to the principal axes of zero-field splitting and g-tensor.

A(S_{Fe} = 3/2)/$g_N\beta_N$ = (−3.62, −19.47, +0.30) T, with A_{iso}-(S_{Fe} = 3/2)/$g_N\beta_N$ = −7.60 T. The isomer shift, quadrupole splitting, and hyperfine coupling constants all are in accord with the Mössbauer data determined for related five-coordinate ferric-iodo complexes coordinated by ligand radical dianions.[45,50,51] These compounds, listed in Table 4, also were characterized as intermediate spin ferric species. The electronic structure of **5** is thus represented best by [Fe(↑↑↑)(TIM↓↓)I], with S_{Fe} = 3/2 and S_L = 1; antiferromagnetic coupling between the unpaired metal- and ligand-centered spins gives rise to the doublet, S_T = 1/2, ground state of the molecule. By analogy, the [Fe^{3+}(TIM^{2-})]$^+$ units of compound **4** are assigned an identical configuration.

The EPR spectrum of **5** (Figure 11, bottom) provides further evidence of the electronic structure deduced from the crystal structure and Mössbauer spectroscopy. The anisotropic spectrum displays g values of 2.3076, 2.102, and 2.012. Hyperfine interactions with the iodo ligand (I = 5/2, A = (4, 11, −16) × 10^{-4} cm^{-1}) and a large electric quadrupole contribution (P = (6, −10, 4) × 10^{-4} cm^{-1};

α = 0°, β = 30°, γ = 90°) leads to the observed splitting pattern in the EPR spectrum of **5**. The EPR data, likewise, matches that of the related intermediate spin ferric-iodo complexes (Table 4), in support of the shared electronic structure.

The remarkable outlier in the series of [Fe(TIM*)]$^+$ compounds is the monocationic phosphite complex, **7**. Both the EPR and Mössbauer spectra are in stark contrast to the data obtained for the related series of five-coordinate [Fe^{3+}(L^{2-})]$^+$ and [Fe^{3+}(TIM^{2-})]$^+$ complexes listed in Table 4. The data provides additional evidence of a unique electronic structure for **7**. The crystallographic data for **7** led to the prediction that the formation of the monocationic phosphite complex involves the oxidation of the TIM ligand in **6** rather than of the metal center. Compound **7** would thus consist of a divalent iron center, rather than a ferric ion, as established for **4** and **5**. Two electronic configurations again are plausible for a ferrous description of **7**, denoted by [Fe(↑↓)(TIM↑)]$^+$ and [Fe(↑↑)-(TIM↓)]$^+$. The former representation signifies a low spin ferrous ion, with the unpaired spin resident in a ligand-centered orbital. The latter configuration consists of an intermediate spin Fe^{2+} center, antiferromagnetically coupled to the ligand radical anion. The EPR spectrum

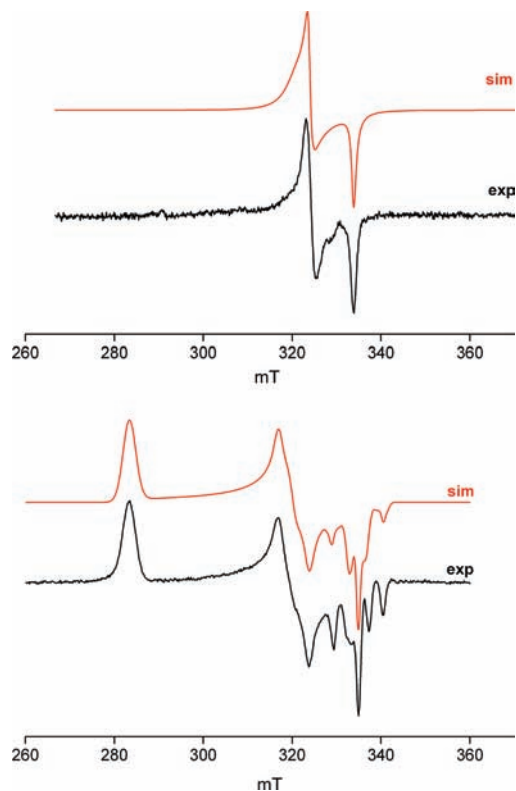(51) Chun, H.; Bill, E.; Weyhermüller, T.; Wieghardt, K. *Inorg. Chem.* **2003**, *42*, 5612.

Figure 11. Bottom: EPR spectrum of **5**, as frozen solution in THF/toluene, 20 K, Microwave frequency 9.4303 GHz, 6 μW power, 5 G modulation amplitude; Top: EPR spectrum of **7** as frozen solution in THF, 15 K, Microwave frequency 9.4326 GHz, 0.1 mW power, 10 G modulation amplitude.

of **7** (Figure 11, top) displays a much tighter range of g values in comparison to the EPR spectrum of **5**, and is best fit with $g = 2.10, 2.08$, and 2.02.[52] However, the values are in accord with either a low-spin or intermediate spin Fe^{2+} description. The isomer shift afforded by the Mössbauer spectra is comparable to the values observed for both **4** and **5**. However, the very small quadrupole splitting, $\Delta E_Q = -0.35$, is indicative of minimal charge asymmetry at the iron center and thus favors a low-spin Fe^{2+} species. The magnetic Mössbauer spectrum (Figure 12) for the cationic complex corroborates the low-spin iron configuration. The small hyperfine coupling constants obtained from the fit of the data, $A(S_T = 1/2)/g_N\beta_N = (-0.43, +1.05, +0.20)$ T, contrast with the values obtained for compounds **4** and **5**. The values indicate minimal charge density at the iron center, which would be consistent with the presence of a low-spin ferrous ion ($S_{Fe} = 0$) in **7**.

DFT Computational Studies. Density functional theory (DFT) calculations (B3LYP functional) were carried out on the synthetic Fe(TIM*) compounds, **4**−**7**, to further resolve aspects regarding their electronic structure. For all compounds, the bond lengths of the geometry optimized structures match well with the crystallographically determined bond distances, and the calculated Mössbauer parameters agree reasonably well with experimental values

(52) The EPR spectrum appears to be concentration dependent: at higher concentrations (> 100 μM), a minor second component is apparent in the EPR spectrum. The origin of the observed spectral changes is not known. No differences are observed in the Mössbauer spectrum of solid samples of **7** vs frozen solutions in THF, suggesting that the electronic structure of **7** remains the same in solution.
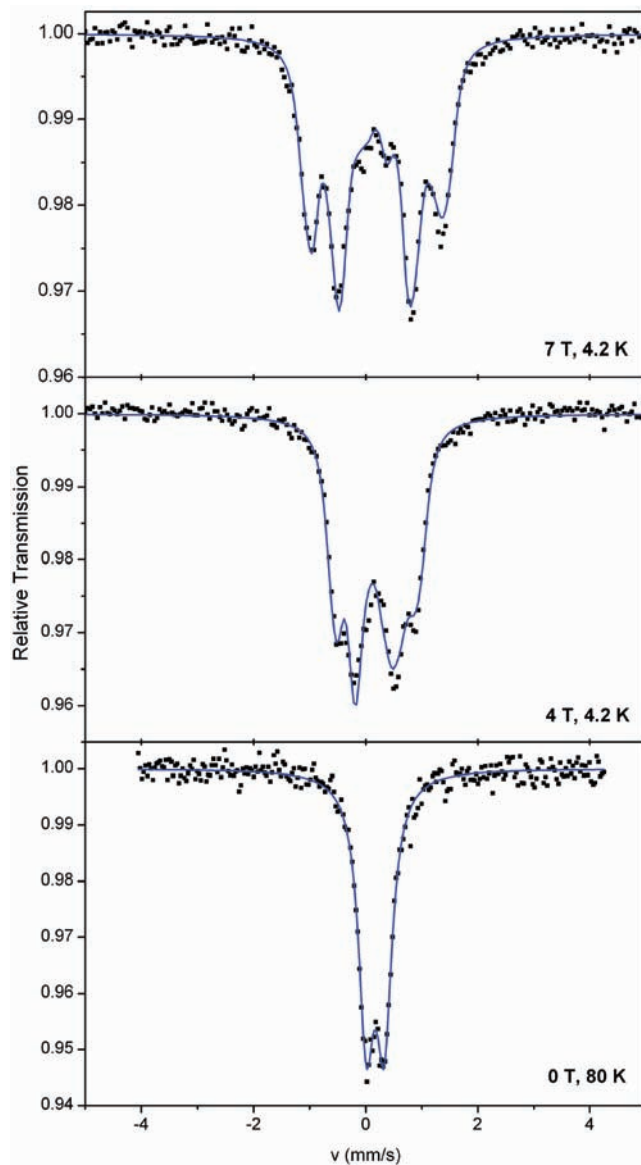

Figure 12. Zero-Field (0 T, 80 K) and applied-field Mössbauer spectra (4−7 T, 4.2 K) of **7**. Experimental data shown as black squares. Fit of the data (solid blue line), $S_T = 1/2$, affords: $\delta = 0.17$ mm/s, $\Delta E_Q = -0.35$ mm/s, $\eta = 0.78$, $g_x = g_y = g_z = 2.00$, [A/$g_N\beta_N$]: $A_{xx} = -0.43$ T, $A_{yy} = +1.05$ T, $A_{zz} = +0.20$ T. Isomer shift relative to α-Fe at 298 K.

(Supporting Information, Table S1). For the binuclear $[\{Fe^{3+}(TIM^{2-})\}_2(\mu\text{-OH})]^+$ complex, **4**, substantial electron delocalization over the various ligand-centered and metal-centered orbitals, coincides with highly complex orbital depictions that obscure a clear assignment of the electronic structure of this binuclear complex. To obtain a simplified molecular orbital (MO) picture for this compound, we therefore calculated the electronic structure of the homologous mononuclear $[Fe(TIM^*)(OH)]$ species ($S_T = 1/2$), which represents the core half-unit of **4**, and likewise, consists of the monocationic $[Fe(TIM^*)]^+$ species. The DFT-derived electronic structure is consistent with the $[Fe(\uparrow\uparrow\uparrow)(TIM\downarrow\downarrow)]^+$ configuration deduced from the crystal structure and the spectroscopic data for **4**. The qualitative MO diagram, shown in Figure 13, reveals three unpaired electrons that reside in the metal-centered d_{xz}, d_{yz}, and d_{z^2} orbitals, which account for the $S = 3/2$ spin state at the Fe
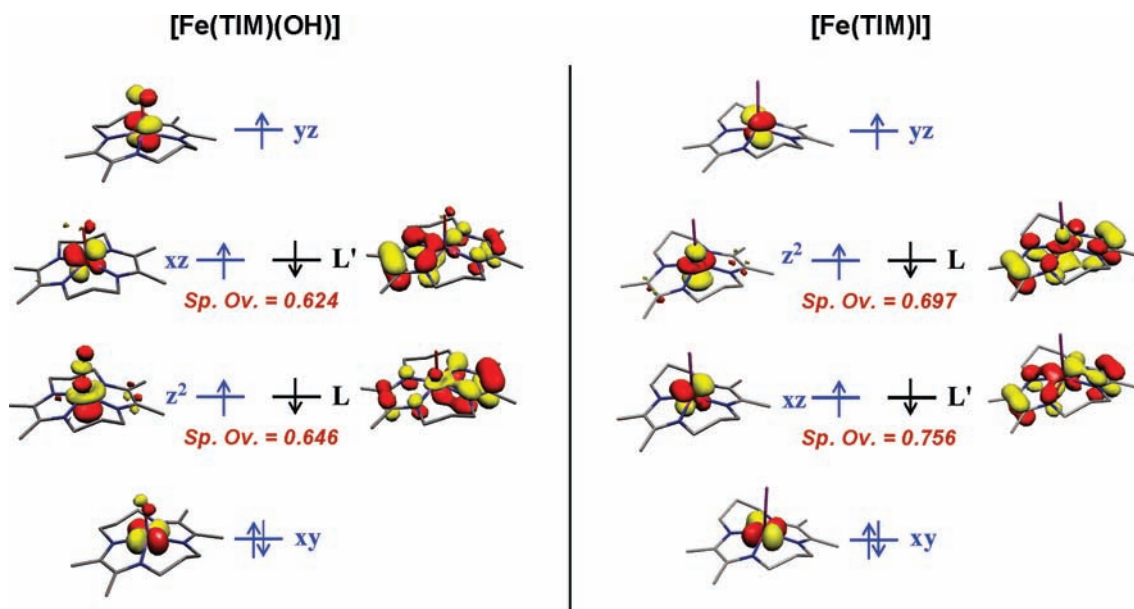
Figure 13. DFT-derived (B3LYP) qualitative MO diagram for [Fe(TIM*)(OH)] and **5**. Spatial overlap (Sp. Ov.) indicated; z-axis along axial Fe−OH and Fe−I bonds.

center. Two singly occupied ligand centered orbitals also are apparent. The non-integer values for the spatial overlaps between the ligand and metal-centered SOMOs (singly occupied MOs) are indicative of strong antiferromagnetic coupling, which accounts for the doublet ground state of the molecule. The DFT-derived molecular orbital diagram for [Fe(TIM*)I] (**5**, Figure 13) is virtually identical to that of the monomeric Fe-hydroxy species, and describes an analogous [Fe(↑↑↑)(TIM↓↓)I] ($S_{Fe} = 3/2$, $S_L = 1$, $S_T = 1/2$) configuration.

DFT results on the neutral [Fe^{2+}(TIM^{2-})(P(OPh$_3$))] compound indicate that, of the two possible electronic configurations in question, [(Fe↑)(TIM↓)] or [(Fe↑↑)(TIM↓↓)], the former description, containing a low-spin Fe^{2+} center, is more accurate. The doubly occupied ligand-centered orbital also denotes closed-shell character for the dianionic ligand (Figure 14). The electronic structure of **6** differs from the calculated structure of the theoretical four-coordinate [Fe(TIM*)]^0 species, which described an intermediate spin Fe^{2+} configuration (Figure 4). The presence of the axial phosphite ligand appears to favor a low-spin iron center.

The results of DFT calculations on the cationic [Fe(TIM*)-(P(OPh$_3$))]$^+$ compound are less clear-cut, and do little to resolve the ambiguity regarding the electronic structure of this distinctive complex. The DFT calculations carried out on the crystal structure, as well as on the geometry optimized (BP86 and B3LYP) structures, suggest two plausible electronic configurations for **7**, that are analogous to the possible low spin ([Fe(↓)(TIM↑)]$^+$) or intermediate spin ([Fe(↑↑)(TIM↓)]$^+$) ferrous structures inferred from the experimental data, and that differ in energy by a mere 2−5 kcal/mol (Supporting Information). The bond distances of the BP86 and B3LYP optimized structures both are in close agreement with the experimentally determined bond lengths for **7**, with the Fe−P distance more accurately replicated in the BP86 optimized structure. The lowest energy solution obtained from calculations (BS2,1) of the B3LYP geometry optimized [Fe(TIM*)(P(OPh$_3$))] structure represents the intermediate spin ferrous species ([(Fe↑↑)(TIM↓)(P(OPh$_3$))]$^+$ (Supporting Information). However, this description conflicts with the

Mössbauer data, denoting negligible charge asymmetry and charge density at the metal center. The MO picture that is most consistent with the spectroscopic data is shown in Figure 14, and illustrates the lowest energy solution derived from calculations (UKS) on the unoptimized or BP86 geometry optimized structure. The calculated Mössbauer parameters for this structure ($\delta = 0.19$ mm/s, $\Delta E_Q = -0.85$ mm/s) also are comparable to experimental values, whereas the calculated quadrupole splitting value for the intermediate spin configuration is much larger ($\Delta E_Q = +1.4 - 1.5$ mm/s), and of opposite sign. Three doubly occupied metal d-orbitals are apparent in the MO scheme; the single electron that accounts for the doublet, $S_T = 1/2$, ground state of the molecule occupies a highly covalent orbital with significant metal and ligand character. The high d-occupancy of this SOMO (34% d$_{z^2}$, 50% d$_{(total)}$ based on orbital population analysis) obscures a clear assignment of this orbital as either metal- or ligand-centered. Thus, the electronic structure of **7** can be described as either a low-spin ferrous compound [Fe^{2+}(TIM^{1-})(P(OPh$_3$))]$^+$, in which the Fe^{2+} center is coordinated by the TIM^{1-} ligand radical anion, or alternatively, as an Fe^I complex. This latter description, represented by [Fe^{1+}(TIM^0)(P(OPh$_3$))]$^+$, denotes the presence of the fully oxidized, neutral form of the ligand (TIM^0). In this scenario, the substantial ligand character of the SOMO signifies backbonding from the diimine π^* orbitals into the Fe d$_{z^2}$ orbital. π-backbonding would also account for the C$_{im}$−C$_{im}$ and C$_{im}$−N$_{im}$ bond distances of the TIM* macrocycle in **7**, which deviate from the expected bond lengths for the neutral, fully oxidized, TIM^0 ligand. The experimental and DFT-derived Mössbauer values for **7** are comparable to the Mössbauer values reported for the five-coordinate monovalent Fe complex, [PhTt^{tBu}]Fe(CO)$_2$ ($\delta = 0.21$ mm/s, $\Delta E_Q = 0.47$ mm/s, 100 K), in further support of the Fe^I formulation of **7**.[53] Significant π-backdonation from the carbonyl ligands of the reported [PhTt^{tBu}]Fe(CO)$_2$ also account for the low isomer

(53) Mock, M. T.; Popescu, C. V.; Yap, G. P. A.; Dougherty, W. G.; Riordan, C. G. *J. Am. Chem. Soc.* **2008,** *47*, 1889.
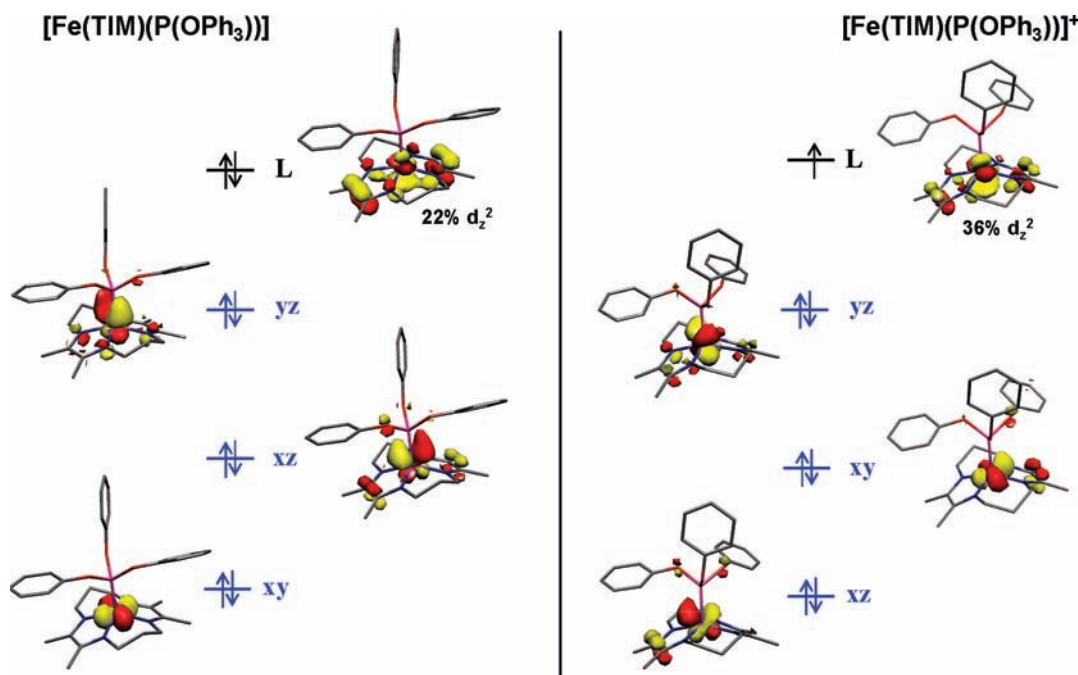
Figure 14. DFT-derived (B3LYP) qualitative MO diagram for **6** and **7**. Spatial overlap (Sp. Ov.) indicated; z-axis along axial Fe−P bonds.

shift values for this monovalent complex, in comparison with other reported Fe^I compounds.[54,55]

Conclusions. The series of calculated [Zn(TIM*)]^n and [Fe(TIM*)]^n structures, and the synthetic Fe(TIM*) compounds described in this work definitively illustrate the redox non-innocence of the macrocyclic ligand, and further advocate the need to reconsider the redox chemistry of diimine-based ligands in the chemistry of their inorganic compounds. The preferential reduction of the TIM ligand, versus of the metal center, already is implied by DFT results on the [Fe(TIM*)]^n species, which encompasses a range of ligand oxidation states starting from the neutral TIM^0, through the trianionic TIM^{3-}; yet in each case, the metal center remains in the divalent oxidation state regardless of the overall spin state of the molecule. Among the synthetic compounds, **3**−**7**, the crystallographic and spectroscopic data also confirm the presence of reduced TIM ligands. The two-electron reduction of [Fe(TIM*)(MeCN)$_2$](PF$_6$)$_2$ involves the macrocycle and yields the Fe−Fe dimer, [Fe$^{2.5+}$(TIM$^{2.5-}$)]$_2$, as previously described.[19] The addition of a phosphine donor (P(OPh)$_3$) to this dimeric complex breaks the metal−metal bond, yet again, the resultant neutral monomeric compound consists of a ferrous ion coordinated by the dianionic TIM^{2-} form of the ligand.

Interestingly, unlike in the computational series of Fe(TIM*) molecules, the oxidation of both **3** and **7** (via the reaction with I$_2$, O$_2$, or Fc*PF$_6$) removes one electron from either the metal or the ligand center, depending on the nature of the axial ligands. Thus, the monomeric iodo complex, [Fe^{III}(TIM^{2-})I], and the μ-hydroxy dimer, [{Fe^{III}(TIM^{2-})}$_2$(μ-OH)](PF$_6$), both contain ferric ions coordinated by the dianionic ligand. In contrast, the oxidation of **6** appears to be ligand centered.

The majority of the experimental data for the synthetic Fe(TIM*) compounds establishes a ferrous or ferric description for these complexes, rather than as low valent Fe^I or Fe^0 species.[14] No evidence exists at all for an Fe^0 oxidation state

among the complexes we have examined. However, the spectroscopic data and DFT results for compound **7** indicate that this cationic Fe-phosphite complex possesses some Fe^I character. For this complex, we cannot explicitly assign an electronic configuration and oxidation states for this complex.

Notably, the series of compounds that we have examined demonstrate that the α-diimine macrocyle is able to stabilize a range of metal and ligand oxidation states. The results suggest that the redox properties of these macrocyclic diimine compounds are "tunable", dependent on the nature of the axial ligands (and presumably also would be influenced by pendant groups on the macrocycle). In general, ligand-centered redox processes will always compete with metal-centered reduction in these compounds, precluding the formation of low valent metal complexes. However, given the appropriate choice of ligand environment, formation of an Fe^I complex in these type of systems is not entirely out of the question, as evidenced by our analysis of compound **7**. The electron storage potential of the macrocyclic ligand and the tunable redox states of these compounds should be useful features to exploit for reactivity. These aspects warrant further investigation into the properties and reactivities of metal coordinated α-diimine based macrocyclic compounds.

Supporting Information Available: Additional spectroscopic information, Mössbauer, electrochemical, and magnetic susceptibility data, and results of DFT computational analysis, as noted within the text. This material is available free of charge via the Internet at http://pubs.acs.org.

(54) Mashiko, T.; Reed, C. A.; Haller, K. J.; Scheidt, W. R. *Inorg. Chem.* **1984**, *23*, 3192.

(55) Hendrich, M. P.; Gunderson, W.; Behan, R. K.; Green, M. T.; Mehn, M. P.; Betley, T. A.; Lu, C. C.; Peters, J. C. *Proc. Natl. Acad. Sci. U.S.A.* **2006**, *103*, 17107.